

Fabrication and Properties of Novel Polymer-Metal Composites Using 3D Printing

A Major Qualifying Project Report
Submitted to the Faculty of
Worcester Polytechnic Institute
in partial fulfillment of the requirements for the
Degree in Bachelor of Science
in
Mechanical Engineering
by

Daniel Braconnier
Kristin Markuson
Mila Maynard

Date: 04/27/2017

Advisors:

Professor Amy M. Peterson (Chemical Engineering)

Professor Diana A. Lados (Mechanical Engineering)

Professor Germano S. Iannacchione (Physics)

Acknowledgments

We would like to thank Matthew Ryder (ME), Anthony D'Amico (CHE), Xuejian Lyu (MTE), Roger Steele (PH), and Russ Lang (CE) for their assistance with lab equipment. Also, our thanks go to Mr. Ian Donaldson of GKN Sinter Metals for providing the stainless steel powders used in this study.

Abstract

This project investigated the novel fabrication and properties of polymer-metal composites (PMCs) using 3D printing (fused filament fabrication–FFF). Mechanical and physical properties of acrylonitrile butadiene styrene (ABS)–stainless steel PMCs (with 5,10,15, and 23 wt% stainless steel powder additions) were generated and compared with those of the base ABS. Tensile testing, dynamic mechanical analysis, differential scanning calorimetry, optical microscopy, and scanning electron microscopy were employed to characterize all materials/conditions. A new methodology to fabricate the composites was first developed. The resulting materials were then extruded into PMC filaments, which were further used to print tensile specimens. Controlling printing parameters, deposition layout and orientation were systematically investigated in order to optimize the process (minimize porosity and enhance homogeneity and interlayer bonding) and improve materials' properties. The results demonstrate feasibility of using 3D printing to create PMCs with increased functionality (magnetic and conductive properties), while preserving or enhancing their mechanical properties.

Executive Summary

Many have tried to blend polymers and metal powders together, yet failed to create a composite mixture worth pursuing. In order to change this, a novel process was created for producing such composites. A composite mixture was chosen to be of acrylonitrile-butadiene-styrene (ABS) and 420 stainless steel (SS) particles at varying SS concentrations suspended in the ABS matrix. The aim was to create composites of ABS and SS particles with great homogeneity. Achieving this allowed for production with an easily controllable material, with hopes of bringing ABS to a more structural stage.

The process for creating our composites began with dissolving ABS pellets in acetone. Once the plastic dissolved, metal particles were added and the solution was mixed. The solution had to have a viscosity that would allow for uniform dispersion. If a solution was too thin, the metal particles would sink to the bottom and it would be difficult to mix. After the material was mixed, it was put on foil and dried. An oven was then used to get the acetone to evaporate.

The next step was the fragmentation and extrusion process. The fragmentation process for the dried material was done manually, the plastic was cut into pieces small enough to go through the extrusion process. It was determined that putting filament into the extruder more than once decreased porosity and increased dimensional accuracy. The next step was using the filament in a Hyrel 30M 3D printer. There were many parameters of 3D printing that were taken into consideration during this project. In order to make sure that tensile bars were having similar thermal behaviors in between layers, a thermal camera was also used. This was to ensure that a printed layer had time to cool, but was still hot enough to bond with the next printed layer. The final step was tensile testing. The tensile bars that were printed were pulled with an Instron machine. We were able to determine tensile strength, ductility, and young's modulus from this experiment.

There are many printing parameters explored for manufacturing the tensile bars. The plain ABS was optimized before the composite. Preliminary studies were performed on the print and fan speeds as well as the layout of the tensile bars in the build chamber. The primary focus was on stainless steel weight percent, filament uniformity, print orientation, and raster orientation.

The weight percent of stainless steel in the ABS was varied between 0 and 23 weight percent, and the particle distribution in these composites was observed to be uniform. The filament uniformity refers to both the diameter of the extruded filament and the absence of porosity in the filament. The print orientations were two consistent variables: half of the bars tested were printed vertically and the other half horizontally. The raster orientation was the final parameter: how the infill pattern of the bar is printed. Half of the bars were made with 0/90° raster orientations (rotating 90° on adjacent layers) and the other half was made with -45/45° raster orientations. All of these parameters were thoroughly explored to improve the fracture surfaces. Initially, the fracture surfaces established the weak interlayer and infill bonding and many voids. The optimized fracture surfaces were much improved; showing no voids and strong bonding.

Optimizing our processes up through printing resulted in materials that had average mechanical properties 40% greater than found in previous literature. Having a high Ultimate Tensile Strength (UTS) is important for a material to act better structurally in different situations. This project was able to preserve the properties of the base material in our ABS-SS composites of 10 through 15 weight percent.

It was found that the process of 3D printing affected the percent elongation (ductility) of our material. The vertically oriented bars experienced on average a 76% decrease in ductility compared to the horizontal print orientation. This can be attributed to the fact that a vertically printed bars when tensile tested are subject to a force that is normal to the printed layer plane. ABS-SS composites of SS concentrations 10 and 15 wt% showed an increase in elastic modulus compared to the raw ABS prints. This increase then changed to a decrease at a SS concentration of 23 wt% (ultimately decreasing by 10%); which shows a potential inflection point where the SS concentration in ABS starts to drastically decrease from original properties.

Differential scanning calorimetry was used to observe and compare the thermal behavior of the different materials. Heating and cooling runs on this test reaffirmed the homogeneity of our materials because of the uniform phase transitions. The amount of SS particles in the material lowered the shift in heat capacity after the glass transition temperature.

The composite with thermal behavior closest to plain ABS was the 15% PMC. This also corresponds to the 10 and 15% composite results that had a UTS within 4.4% of the plain ABS. This means that we were able to achieve a composite that had similar mechanical and thermal properties to ABS which is a very promising result.

Dynamic mechanical analysis is a process executed to understand the viscoelastic behavior of the materials as a stress is applied. As seen in the graph, the raw ABS and the 10% ABS behaved the same in the testing and therefore the 10 weight percent SS was the most effective in maintaining the properties of ABS while also having a filler.

Overall, by using a thermal camera a g-coded printing process was created to produce print specimens with unprecedented mechanical properties and very low filament porosities. Furthermore, being able to create a polymer-metal composite with mechanical properties that rival a print of the plain base material opens many doors to research on this topic. Having composite materials of similar properties means they can be used in various situations for their now added functionality.

This project can be used as a first step into research for 3D printing composite materials with enhanced properties and functionality. Composites with different metal powders and different weight percentages could yield more unique properties. Functionalizing powders could lead to metal particles that achieve better bonding with the polymer matrix.

Exploring these fields could lead to materials with increased thermal and electrical conductivity. Enhanced mechanical properties and even magnetic properties can be achieved. These materials could have customizable characteristics for applications in prototyping and much more. Through this project's success, there is the potential for composite functionality within additive manufacturing for structural applications.

Table of Contents

Acknowledgments	i
Abstract	ii
Executive Summary	iii
List of Figures	vii
List of Tables	ix
Introduction	1
Chapter 2: Literature Review	5
2.1 Bond Formation During Fused Filament Fabrication	5
2.2 Process Parameters	6
2.2.1 Build Orientation	6
2.2.2 Raster Orientation	6
2.3 Polymer-Metal Composites	8
Chapter 3: Methodology	10
3.1 Materials	10
3.2 Composite Preparation	10
3.2.1 Protocol to Dissolve Plastics & Composites	10
3.2.2 Composite Drying	11
3.2.3 Filament Extrusion	11
3.3 Print Tensile Bars	12
3.3.1 How to Use 3D Printer	12
3.3.2 Horizontal vs Vertical Prints and Raster Orientations	13
3.3.3 Optimization of Print Parameters	13
3.3.4 G-Code Modifications for Single Bar Prints	14
3.3.5 Printing Tensile Bars	15
3.4 Materials Characterization and Testing	15
3.4.1 Tensile Testing	15
3.4.2 Differential Scanning Calorimetry	17
3.4.3 Dynamic Mechanical Analysis	17
3.4.4 Scanning Electron Microscopy	17
Chapter 4: Results and Discussion	19
4.1 Optical Microscopy of the Processed Composites	19
4.2 Differential Scanning Calorimetry	19
4.3 Extrusion	22
4.4 Dynamic Mechanical Analysis	24

4.5 Optimization of the Printing Process and Parameters.....	25
4.6 Tensile Properties and Optimization.....	26
4.7 Fractography Using Scanning Electron Microscopy (SEM).....	30
4.8 Added Functionality of Polymer-Metal Composites	39
Conclusions	40
Bibliography	41
Appendices	i
Appendix A: G-Code for Single-Bar Prints	i
Slic3r Program	i
Macro G-Code Editor Script	iv
Appendix B: DSC	vii
Thermographs of Functionalized Steel	vii
Heating and Cooling Numerical Data from DSC Tests	viii
Nylon-6 Thermograph.....	ix
Appendix C: Explorations with Nylon-6	x
Appendix D: Average Tensile Data Tables.....	xii

List of Figures

Figure 1: Growth of rapid prototyping [2].	1
Figure 2: FFF representation [3].	1
Figure 3: (a) Part printed with a perimeter, (b) part printed only with the raster pattern.	2
Figure 4: The left side shows the different raster orientations in vertical prints, while the right shows the different orientations in horizontal prints.	3
Figure 5: Particles that are being sintered together at a high temperature [7].	5
Figure 6: Build orientation terminology: (a) vertical bars, (b) horizontal bars.	6
Figure 7: Raster angles of the samples.	7
Figure 8: Tensile strength for Iron-ABS-Binder composite [16].	8
Figure 9: Additives: (a) jute fibers, (b) TPE, and (c) TiO ₂ [13].	9
Figure 10: The Filabot extruder and spooler working together to produce filament.	11
Figure 11: A Hyrel System 30M Printer used for fused filament fabrication.	13
Figure 12: (a) shows the bars when printed in a straight line and (b) shows the bars when printed in a pentagon.	14
Figure 13: A labeled set of white ABS -45/45 H tensile testing bars (a) and the results of a tensile bar passing a tensile test with a fracture within the specified gage length (b).	16
Figure 14: The Instron 5567A was used for tensile testing.	16
Figure 15: Edge of ABS-SS23 at 5× magnification (a), (b) center of a batch of ABS-SS23 at 20× magnification. The scale bars for both micrographs represents 50 μm.	19
Figure 16: The graph of the first trial of ABS-SS23 (a) that shows non-uniformity caused by remaining acetone. The graph of the second trial of ABS-SS23 (b) which has a more uniform and reproducible pattern.	20
Figure 17: Shows DSC heating (a) and cooling (b) cycle data from ABS and ABS-SS composites.	21
Figure 18: Shows DSC heating (red) and cooling (blue) cycle data from ABS and ABS-SS composites.	22
Figure 19: The micrograph (a) is the ABS-SS23 filament after one pass through the extruder. The micrograph (b) is the ABS-SS23 after a second pass through. The scale bars for both micrographs represents 200 μm.	23
Figure 20: Dynamic mechanical analysis results showing the similar properties between the raw ABS and the ABS-SS10.	24
Figure 21: Representation of where each value of a mechanical property was collected from [10].	27
Figure 22: A comparison between batches 1 through 4 to assist in the optimization process of the printing parameters.	27
Figure 23: A comparison between the best tensile tests of the 0/90 V orientation in all compositions.	28
Figure 24: The UTS values collected for each print orientation and material composition.	29
Figure 25: The percentage elongation (ductility) values collected for each print orientation and material composition.	29
Figure 26: The Young's modulus values collected for each print orientation and material composition.	30
Figure 27: The red circle indicates where SEM samples were taken when taken from vertical bars when taken off of the print bed. The line on the bottom represents the print bed.	30
Figure 28. SEM images of Factory ABS fracture surfaces at low (a,c,e,g) and high (b,d,f,h) magnification.	32

Figure 29. SEM images of ABS fracture surfaces at low (a,c,e,g) and high (b,d,f,h) magnification.	33
Figure 30. SEM images of ABS-10%SS fracture surfaces at low (a,c,e,g) and high (b,d,f,h) magnification.	34
Figure 31. SEM images of ABS-15%SS fracture surfaces at low (a,c,e,g) and high (b,d,f,h) magnification.	35
Figure 32. SEM images of ABS-23%SS fracture surfaces at low (a,c,e,g) and high (b,d,f,h) magnification.	36
Figure 33: Micrograph of ABS-SS10 -45/45 H at 330× magnification distinctly shows the particles within the polymer matrix. Some of the metal particles are presented in the red circles. Hackle markings are shown within the blue circle.....	37
Figure 34: Micrograph of cross section of ABS-SS10 -45/45 H SEM sample.....	38
Figure 35: The tensile results of ABS-SS10 -45/45 V bar 1 (a) and 2 (b).	38
Figure 36: Micrographs of cross sections of ABS-SS10 -45/45 V bar 1 (a) and 2 (b).....	39
Figure B1: <u>Graph that compares the change in heat capacity of normal ABS-SS10 to ABS-SS10 using functionalized steel during a heating cycle.....</u>	viii
Figure B2: <u>Graph that compares the heat capacity of normal ABS-SS10 to ABS-SS10 using functionalized steel during a cooling cycle.....</u>	ix
Figure B3: The results of heat capacity during the heating and cooling cycle of dried Nylon-6.....	x
Figure C1: <u>Stress-Strain curves for the four Kevlar fiber reinforcement configurations [18].....</u>	xi

List of Tables

Table 1: Tensile data from literature of pure ABS [11-15].....	7
Table 2: Extrusion Temperatures for Neat and Composite Materials.....	23
Table 3: C-Factor values indicating the stiffness of the material in comparison to the raw ABS.....	24
Table 4: Optimized printing parameters for both ABS and ABS-SS, the only thing altered being the maximum fan speed for horizontal prints and vertical prints.....	25
Table D1: Comparing averages from tensile tests of the 0/90 H prints of each material.....	xii
Table D2: Comparing averages from tensile tests of the -45/45 H prints of each material.....	xii
Table D3: Comparing averages from tensile tests of the 0/90 V prints of each material.....	xii
Table D4: Comparing averages from tensile tests of the -45/45 V prints of each material.....	xii

Introduction

Additive manufacturing (AM), a form of rapid prototyping, offers many advantages including reduction of cost and time, a product development cycle, and the possibility of creating shapes that are difficult or impossible to machine. These advantages have led to the use of AM for aircraft and aerospace applications as well as architectural modeling and medical applications [1]. The growth of rapid prototyping can be shown in Figure 1.

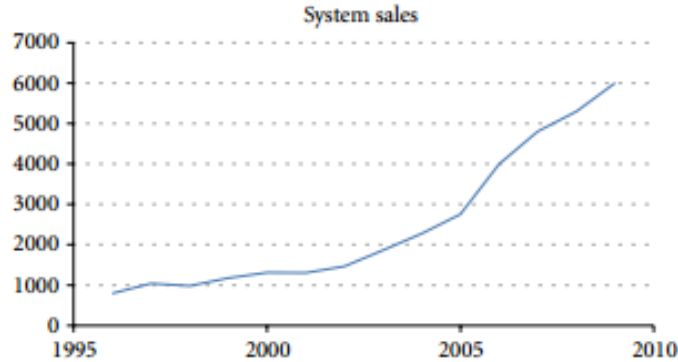


Figure 1: Growth of rapid prototyping [2].

Due to increased industrial interest in AM, research has focused on finding more applications, developing new materials, and improving the processes of fused filament fabrication (FFF) [2]. FFF additive manufacturing uses melted or softened materials to produce each layer while printing. A depiction of FFF can be found in Figure 2.

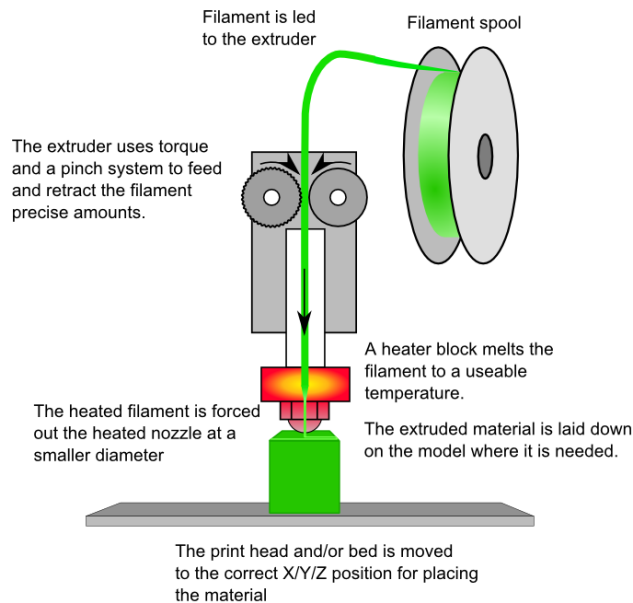


Figure 2: FFF representation [3].

The common materials used in FFF are acrylonitrile butadiene styrene (ABS), polylactic acid (PLA), nylon, and various glass filled nylons. Within this project, ABS is used for different purposes. ABS is the most common polymer in FFF due to its average mechanical properties. This makes ABS an excellent choice for models and prototypes. ABS is a versatile material which has the ability to be sterilized, have an increased transparency, and have increased electrostatic dissipativity [4]. Filaments used for FFF are created by the extrusion of thermoplastic polymers. The polymers start as pellets, granules, or powders in a hopper. The particles are then fed into the barrel of the extruder and an internal screw starts to push the polymer through the barrel to the die. Barrel heaters and mechanical friction from the screw(s) is used to liquefy the polymer material [5].

There are many variables to consider when using an FFF machine such as temperature, speed, and how the part is built. The print head temperature as well as the print bed temperature must be set to melt the filament to the most suitable viscosity and adhere the filament onto the bed. These temperatures will vary from material to material. Fans are also in FFF machines and their speeds can be altered to help with the cooling rate of the printed material. The speed of the print head is also closely related to how the part cools.

The printing protocol is very important when using FFF machines. These protocols may include programming print parameters, build direction, or patterns. Parts can be produced with or without a perimeter, as seen in Figure 3. The direction in which the interior of the parts is built is called the raster orientation. Examples of different raster orientations can be seen in Figure 4. Layer infill is the proximity of the lines of material that the printer extrudes. Infill is the density of the part.

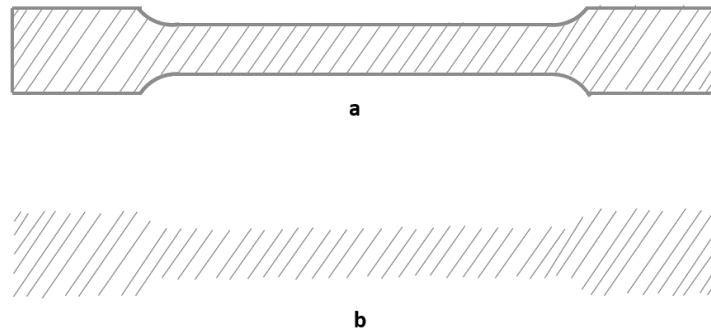


Figure 3: (a) Part printed with a perimeter, (b) part printed only with the raster pattern.

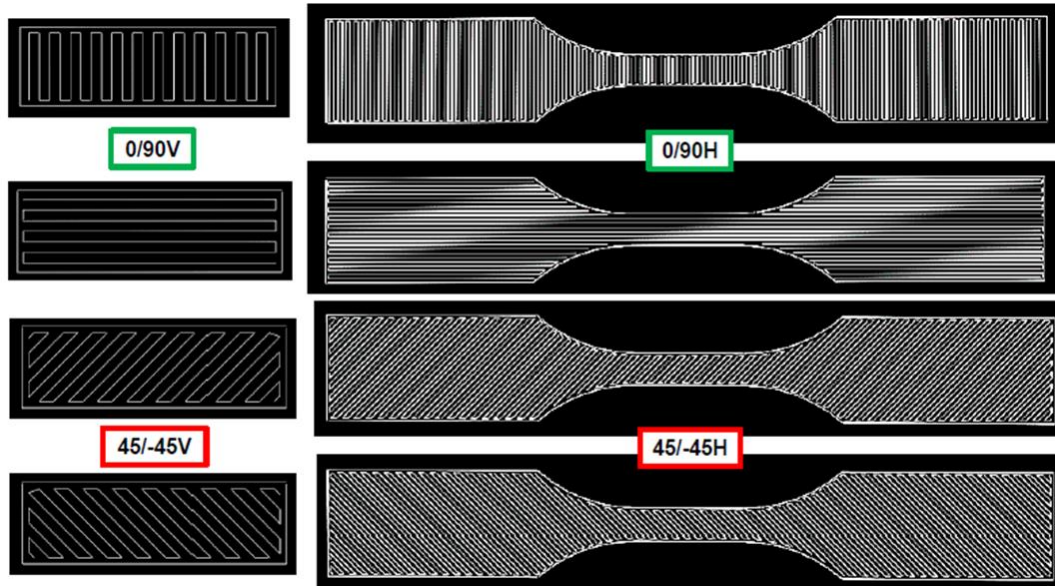


Figure 4: The left side shows the different raster orientations in vertical prints, while the right shows the different orientations in horizontal prints.

Objects printed by means of FFF are not strong enough to be utilized as a finished part, nor do they achieve the surface finish standards of today's marketed products. The major disadvantage of FFF is the low resolution of its z-axis when compared to other AM processes, meaning that a finishing process may be required to achieve a smooth surface [1]. The FFF specimens can have decreased mechanical properties due to their voids. These voids create a light material that has the opportunity to be improved through control of void geometry and distribution. Taking advantage of filling voids with additives through infiltration or other means can lead to a variety of property improvements [6].

To try and make up for these setbacks, polymer AM is evolving to use polymer composites. Fillers have been added to native print materials to increase their mechanical properties. So far these composites have only been created by adding the fillers directly to the polymer matrix as the filaments are being extruded. Previous research has found that there is a lack of cohesion between the fillers and the polymer matrix, thus resulting in lower mechanical properties.

The overarching goal of this project is to create and produce a polymer-metal composite with enhanced mechanical properties for FFF. The objectives to reach this goal are outlined below.

1. Achieve wetting between the polymer matrix and metal powder:
We hypothesize that increased wetting between the filler (metal powder) and matrix (polymer) will increase the mechanical strength of the composite.
2. Achieve homogeneous dispersion within our composites:
Composite mixtures were created by dissolving the native polymers into solution so as to suspend the filler evenly throughout the mixtures. Having an even dispersion will improve the quality of the printed specimens.
3. Successfully print tensile samples:

Each new composite will have a different set of printing parameters. Some of these parameters include: build orientation, raster orientation, and metal composition.

4. Analyze the mechanical properties of the created composites:

The data from the tensile strength testing was compared to other tests from this project as well as literature values.

The following chapter is a literature review that provides information about projects that have data and findings useful to guide this project. Chapters 3, 4, and 5 discuss the methodology, results/discussion, and conclusions of the project respectively.

Chapter 2: Literature Review

Previous studies on fused filament fabrication (FFF) with composites has led to further understanding of additive manufacturing (AM) and how a material behaves throughout the printing process. Multiple reports assisted in the preparation for this project, providing the behavior of material throughout FFF as well as print parameters to alter. The following sections discuss studies on bond formation, 3D-Printing parameters, and tensile data of AM composites.

2.1 Bond Formation During Fused Filament Fabrication

The report, “*Investigation of Bond Formation in FDM process,*” investigates the heat transfer that the polymer, ABS, undergoes during FFF [7]. In this work, the bond formation between layers of the FFF prototypes are critical in understanding the mechanical properties of material that is used in FDM and the prototypes that it forms. [7]. Li et al. investigated adhesion between polymer filaments during sintering. Their research focused on the sintering process of two cylindrical particles (diameter 470 μm and thickness 300 microns) that were cut from sections of extruded filaments from the FFF machine. Both constant and ramped temperatures were studied. The experiment found that the material degraded rapidly above the temperature of 240°C. Figure 5 shows particles that are being sintered at a high temperature and how they deform over time. The report claims that this deformation may contribute to the thermo-oxidative degradation of the polymer [7]. This experiment is relevant to the current work because the knowledge of bond formation of particles during FFF is critical to this project. The rate and level of wetting that are achieved between polymer filaments are highly dependent on the extrusion temperature and convection conditions. By understanding the relationship between surface wetting and temperatures, this project will be successful.

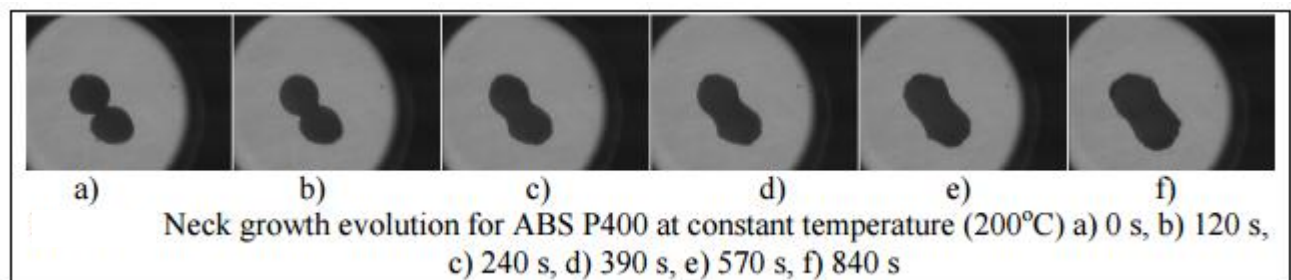


Figure 5: Particles that are being sintered together at a high temperature [7].

2.2 Process Parameters

There are multiple variables that can be changed during the 3D printing process, including travel time, layer thickness, raster orientation, and build orientation. In order to fabricate a sample with high and consistent tensile properties, these parameters were altered to find the best combination that produces the most desirable mechanical properties.

2.2.1 Build Orientation

A major component that has been analyzed through testing is the build orientation, or what direction the sample will be created at. Figure 6 depicts the horizontal and vertical orientations used in experiments.

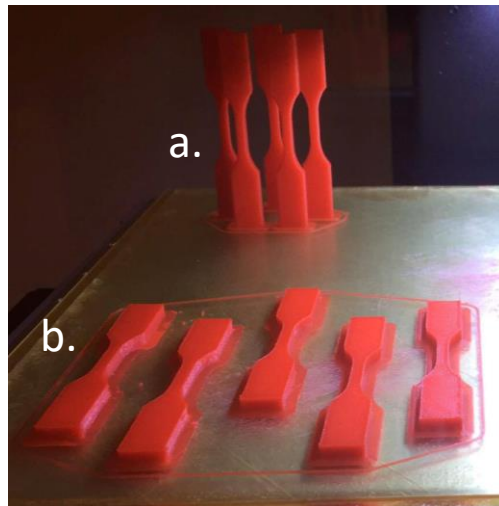


Figure 6: Build orientation terminology: (a) vertical bars, (b) horizontal bars.

The horizontal orientation had higher tensile strength than the vertical [8-11]. This is because the tensile forces are pulling along the beads of filament that are laid on the print.

2.2.2 Raster Orientation

A variable that causes noticeable differences in tensile strength is raster orientation. Raster orientation is the pattern of the internal structure of the additively manufactured part. Studies have been performed to test raster orientations of the same angle per layer, and angles offset by 90° for adjacent layers. Figure 7 depicts the raster orientations studied. It was determined that the raster angles did have an effect on the tensile properties. The findings were that tensile bars with raster angles of 0° (parallel to the direction of tensile testing) had the highest strength. Specimens with an orientation of 90° consistently had the lowest tensile strength. For raster orientations that are

offset by 90° for adjacent layers, it was concluded that the raster orientations of -45/45 created slightly stronger bars than 0/90 [9, 11, 12].

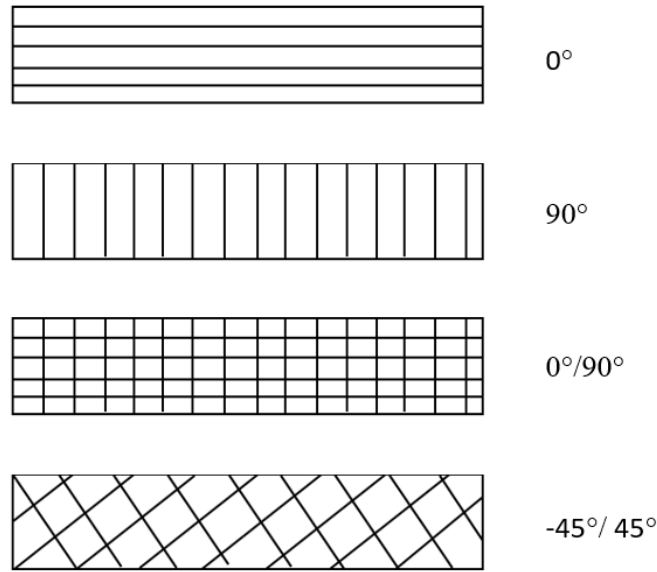


Figure 7: Raster angles of the samples.

Tensile testing is used to measure the mechanical properties of the tensile bars and provides information on which build orientation and raster orientation result in the better properties. The ultimate tensile strength for raw ABS as studied in literature can be seen in Table 1.

Table 1: Tensile data from literature of pure ABS [11-15]

	Author	Orientation	UTS (Mpa)
Pure ABS	Catrell et al.	0/90 V	24.4 +/- 0.5
	Riddick et al.		13.61+/-1.13
	Perez et al.		14.1
	Torrado et al.		17.73
	Catrell et al.	-45/45 V	25.8 +/- 0.3
	Riddick et al.		19.8+/-2.22
	Catrell et al.	0/90 H	29.1 +/- 0.3
	Riddick et al.		25.69+/-1.75
	Perez et al.		28.5
	Torrado et al.		33.96
	Chockalingham et al.		33.94
	Catrell et al.	-45/45 H	28.8 +/- 0.2
	Riddick et al.		27.77+/-0.92
	Ziemian et al.		16.90+/-0.09

2.3 Polymer-Metal Composites

Past studies have analyzed the feasibility of polymer-metal composites for FFF applications. ABS was mixed with iron powder at different concentrations and bound together with surfactant powder material in order to find the effects of iron powder added to the ABS polymer on the material's tensile strength, hardness, and flexural strength. The surfactant binder was added to help maintain homogeneity in the composite and allow for higher amounts of iron powder to be added to the polymer matrix. The homogeneous compound was injection molded into a horizontal NP7-1F molding machine for the tensile and hardness test specimens. The specimens were prepared based on DIN EN ISO 527-2 standards for tensile tests and ASTM D2240 standards for hardness tests. The results of the tensile tests, which can be seen in Figure 8, showed that the polymer-metal composites with increased amounts of palm stearin had increased max stress and break stress. The hardness tests showed that the polymer-metal composite with the most iron powder and surfactant had a significant decrease in flexural properties with a relative increase in hardness. It was also determined that with proper application of surfactant agents, polymer-metal composites of ABS and Iron could be created with more desirable properties for filaments used in FFF [16]. Unfortunately, the combination of ABS and iron did not increase the mechanical properties as expected [16].

Sample	ABS-Palm stearin		ABS-Paraffin wax	
	Max Stress (MPa)	Break Stress (MPa)	Max Stress (MPa)	Break Stress (MPa)
1	5.26	4.70	12.80	12.62
2	7.50	7.36	12.64	12.22
3	9.22	8.72	11.00	11.00

Figure 8: Tensile strength for Iron-ABS-Binder composite [16].

The polymer ABS is amorphous and has no polar characteristics, meaning that it will not interact well with fibrous fillers [16]. Successful addition of metallic powder to ABS represent validity in experimenting further with reinforcing a polymer's native matrix. Though the iron did not increase the UTS of ABS, these results show room for improvement and reasoning to test for different methods of adding the metallic fillers to a polymer matrix.

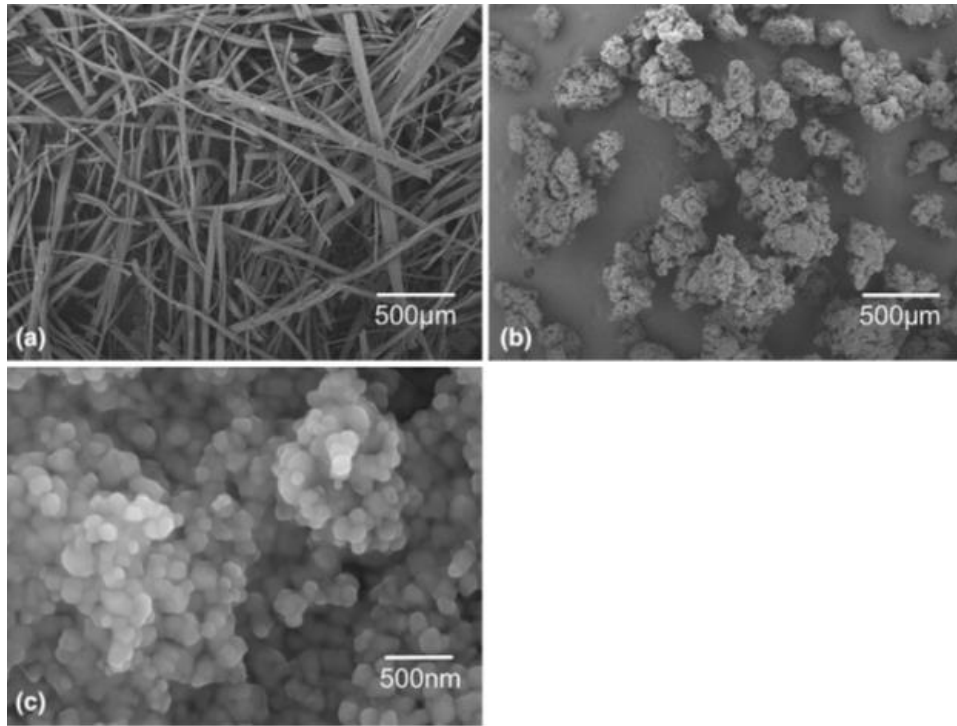


Figure 9: Additives: (a) jute fibers, (b) TPE, and (c) TiO_2 [13].

Tensile specimens were printed using the Makerbot Replicator with an extrusion diameter of 1.77 mm. The various additives used in the ABS composite are shown in Figure 9. The tensile bars were printed to the ASTM D638 standard Type V shape. The tensile tests were done at 23°C with an Instron® 5866 machine equipped with a 10 kN load cell at a speed of 10 mm/min. The ABS/jute fiber composite experienced a 9% lower UTS. The ABS/ TiO_2 composite showed a 13.2% increase in its UTS. The ABS/thermoplastic elastomer (TPE) composite had a reduced UTS by 16%. Contrary to speculation, the addition of additives to the native ABS matrix resulted in fractured surfaces that exhibited brittle characteristics versus the expected ductile behavior. It was also found that parts printed in the ZXY (vertical) direction had a far lower mechanical strength compared to those fabricated in the XYZ (horizontal) direction. This can be attributed to the higher presence of cavities and failure to achieve strong interfaces between layers in the ZXY direction [13]. The success of TiO_2 as a filler in ABS demonstrates that oxides have better wetting or incorporation in the polymer matrix. Surface treatments of metal powders may have a positive effect on their usefulness as a filler. Treating the surface of the powders such that they oxidize could prove beneficial.

Chapter 3: Methodology

3.1 Materials

A 420 Stainless Steel (SS) powder from Hoeganaes Corporation, provided by GKN Sinter Metals, was used as the metallic particulate additions to the ABS polymer matrix. The chemical composition is: carbon 0.29, oxygen 0.33, sulfur 0.010, nitrogen 0.024, chromium 14.0, silicon 0.62, nickel .07, iron and the apparent density is 2.83 g/cm³.

The gas atomized non-spherical powders may offer improved mechanical bonding within the polymer matrix due to surface asperities and general roughness caused by the atomization process. The particles were characterized using the SEM, and the average particle dimensions parallel to the long axis reinforced the information on the provided data sheet, that the average maximum dimension of the particles was around 30 μm.

Acrylonitrile butadiene styrene (ABS) and polylactic acid (PLA) are the most commonly used materials for FFF. Compared to PLA, ABS has greater heat-resistance (up to ~105°C for ABS compared to ~60°C for PLA) and impact-resistance, and has superior machinability. Due to these advantages, ABS was selected as the polymer matrix for the composites in this study. Large spools of factory made ABS filament were used primarily for process optimization, while white ABS pellets were purchased and used as the polymer phase for composites.

Acetone (99.9%, McMaster Carr) was used to dissolve ABS. Dissolution of ABS pellets in acetone began immediately at room temperature. Due to the high vapor pressure of acetone, it readily evaporates at room temperature, resulting in significantly lower drying times than would have been possible with less volatile solvents.

3.2 Composite Preparation

3.2.1 Protocol to Dissolve Plastics & Composites

Through some trial and error, the correct acetone and ABS mixture was found for the optimal solution viscosity. Initially, many ABS and acetone solutions were prepared at varying compositions. The differing amounts of acetone resulted in a range of viscosities, which, in turn, affected how easily the metal powder moved through the solution. It also impacted the suspension stability of the metal powder. An optimum suspension had an even gray color in different intensities depending what amount of SS particles were added. The optimized formulation that produced the best viscosity in ABS was a ratio of 30 g of ABS to 70 mL acetone and the process to dissolve the ABS took approximately 2 days. For composite formulations, 420 stainless steel (SS) powder was mixed into the ABS solution at different weight percentages. Metal powder was added in small increments until oversaturation was noticed. From this weight percentage, smaller

weight percentages were chosen. The weight percentages used throughout this experiment are 5, 10, 15, and 23 wt% of 420 SS.

3.2.2 Composite Drying

Before the solutions with metal powders were dried, they were mixed with an electric mixing screw to ensure solution homogeneity. Once the mixture was uniform, it was poured evenly onto a sheet of aluminum foil and left to dry under ambient conditions in a chemical fume hood. After air drying the composite for at least 4 hours, the composite was put into an oven at 110°C for 4 hours in order to speed up the evaporation of any remaining acetone.

It was critical to note each compositions' metal dispersion under a microscope. It also helped give a better visualization and understanding of the interactions of the composite. This procedure defined a baseline of what the average morphology looks like so that it could be compared to the morphology of the compositions after additional processing and testing.

3.2.3 Filament Extrusion

Once the composite was dried, it was manually fragmented into pieces small enough to undergo the extrusion process. The polymer extruder that used throughout this project was the Filabot Original Extruder. The Filabot has a three stage extrusion screw that is designed to pressurize the plastics during extrusion to help control diameter and boost output. The Filabot utilizes a long compressive section with progressive shear stresses to increase the mixing capability in the barrel. The extruder has a maximum barrel temperature of 450°C. The dried composite sheets were roughly chopped with a desk slicer and scissors. The larger pieces of composite were then manually chopped with scissors to a size the filament extruder would process efficiently, which was approximately $4 \times 4 \times 3 \text{ mm}^3$. The pellets were then loaded into the extruder hopper. Once the extruder reached a set temperature, the pellets were extruded into filament, which was spooled on an automated Filabot Spooler, which can be viewed in Figure 10.



Figure 10: The Filabot extruder and spooler working together to produce filament.

To clean the extruder between different material extrusions, the extruder was heated to 180°C and the extruder die was removed from the machine. The Filabot extruder purge compound, with a higher glass transition temperature (T_g) than the extrusion temperature, was run through the open extruder cavities to clean out the previously extruded neat polymer or composite.

The Filabot extruder/spooler has a variety of parameters that affect how the extruded material and the printed material behave and what its properties are. The desired product of the extruder and the spooler was a filament with as little porosity as possible and with a diameter between 1.66-1.74 mm, with the target diameter being 1.72 mm. The parameters that had the highest impact on the produced filament were the extruder temperature, the spooling speed, the distance between the spooler and the extruder nozzle, and the number of times the material was re-extruded.

Higher temperatures were observed to make the polymers and composites become less viscous and extrude with a decreased filament diameter. The opposite was found from extruding material at lower temperatures. The produced filament would become more viscous and extrude at an increased diameter at lower temperatures. Lower extrusion temperatures were also found to help lower the porosity in the produced filament. The right extruding temperature had to be matched with the proper spooling speed to produce the most uniform results. Specific extrusion parameters for each polymer and composite can be found in results section. It is important to note that the spooler speed was not recordable because there was no RPM readout on the spool used in this report.

3.3 Print Tensile Bars

3.3.1 How to Use 3D Printer

Considering production volume and production time of print specimens for testing, the ASTM D638 Type V tensile bar was selected. These samples would use a minimal amount of material while still generating a final product that would adhere to a reputable standard. A .STL file of the tensile bar was created in Solidworks and then uploaded to Repitrel, the user interface installed on the Hyrel System 30M printer, as seen in Figure 11. In Repitrel, the .STL file was able to be reoriented and repositioned on the print bed. Once placed, the program Slic3r was used to “slice” the .STL file into layers of G-Code, which were used by the printer read to perform the prints.

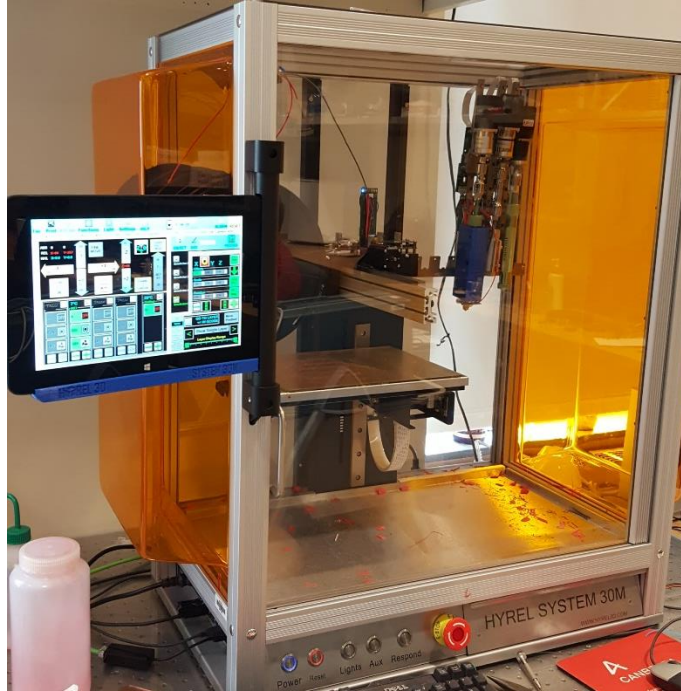


Figure 11: A Hyrel System 30M Printer used for fused filament fabrication.

3.3.2 Horizontal vs Vertical Prints and Raster Orientations

From the literature it is evident that for a single material, there are a wide array of tensile properties that can be obtained solely by varying the raster orientation and build direction of tensile bars. Every other layer is rotated 90° so that there is no anisotropy in the bars with respect to the XY plane, with the only anisotropy resulting from building upwards in the Z direction due to the layers produced in FFF. Build direction refers to the direction that the long axis of the bar is printed in, where horizontal bars are oriented with the long axis flat on the print bed, and vertical bars are oriented with the long axis extending vertically up from the print bed. The resulting orientations mean that horizontally oriented bars have 0 layers perpendicular to the long axis, instead having layer interfaces parallel to the long axis, while vertically printed bars have 0 layers parallel to the long axis and have layers perpendicular to the long axis. In this study, all four cases: -45/45 vertical (-45/45 V), 0/90 vertical (0/90 V), -45/45 horizontal (-45/45 H), and 0/90 horizontal (0/90 H) bars were tested.

3.3.3 Optimization of Print Parameters

Factory-made ABS filament was used for material to find optimized print conditions. The parameters for the composite prints would likely deviate from this ideal print protocol. An idealized pure ABS formulation provided an approximation for the composite print conditions. The first batches of pure ABS prints were five-bar prints, where five tensile bars were printed simultaneously for each of the four configuration patterns tested. The bars were initially positioned

in a straight line 20 mm apart facing the front of the printer, however, after noticing that material tended to ooze out while transitioning from the fifth bar to the first bar (over a 150 mm travel distance), the bars were realigned into a pentagon orientation such that there would be a consistent travel time between all of the bars, Figure 12.

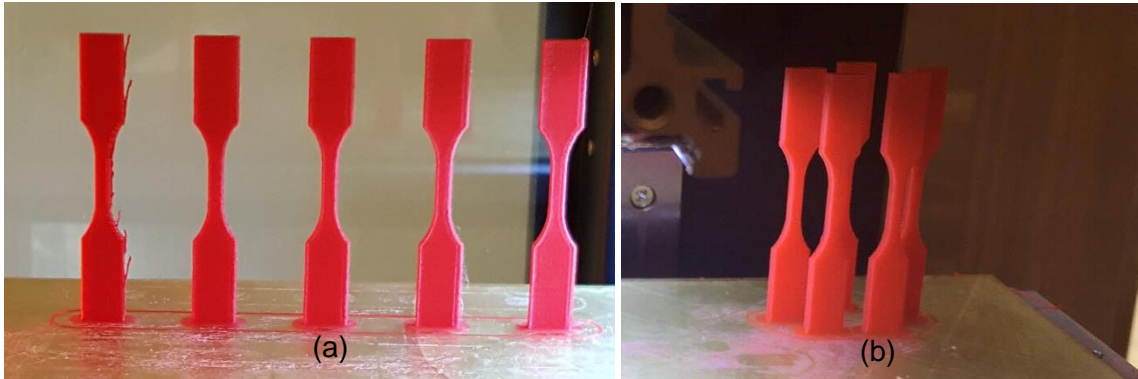


Figure 12: (a) shows the bars when printed in a straight line and (b) shows the bars when printed in a pentagon.

The resulting properties were significantly lower than the values obtained in the literature for pure ABS, especially for the vertical prints. Though there was no porosity in the bars and the printed bars were very dimensionally accurate relative to the initial imported .STL file, the print parameters needed to be optimized more thoroughly to reach literature values.

The tolerance of the extruder, under ideal conditions are rated to ± 0.5 mm with pure ABS. Preliminary 0/90 V single bar prints with pure ABS resulted in bars with extremely low dimensional tolerance adherence, particularly in the gage of the bar, where an oblique gage length formed as opposed to one with a square cross sectional area. It was observed that the layers did not appear to be fully solidified before the following layer was printed on top of it, resulting in the large dimensional inaccuracies. With this problem in mind, a method of increasing the print time for single bar prints was needed.

3.3.4 G-Code Modifications for Single Bar Prints

To make the 0/90 V single bar prints have similar properties to the five bar prints of the same orientation, print times needed to be matched. The Slic3r program was modified to include a skirt around the bar, where a low 2.5 mm/s travel time for the skirt would increase the print time of a single bar print from about 19:30 to 1:28:00. To simulate the print head moving away from the first bar in the print sequence and laying down filament on the other 4 bars, as would be the case in a 5 bar print, the G-Code was imported into Microsoft Excel where a macro was written which added 100 mm all of the X coordinate values in lines of G-Code including the word “skirt” which meant that the print head would move away from the bar before extruding the skirt, which

mimics the time that would have been spent on the other 4 bars in a 5 bar print, before returning to print the next layer on the single bar. A batch of single bar 0/90 V prints were built and tested and the tensile properties were even lower than the 5 bar prints, albeit being dimensionally accurate. A new macro was written which changed all of the “G1” instances in lines of G-Code including the word “skirt” to “G0” which meant that the print head would be told to go to these points, but not to extrude any filament while doing so. The macro would also be easy to modify such that the time away from the bar could be easily tuned, where the goal would be to print as quickly as possible, to facilitate increased interlayer diffusion by laying down layers at as high a temperature as possible, while still maintaining dimensional accuracy. The G-Code for the single-bar prints can be found in Appendix A.

3.3.5 Printing Tensile Bars

Filament adhering to the 1.66-1.74 mm diameter specification of ABS-SS10, 15, and 23 wt% were extruded and printed in accordance to the same finalized 0/90 V, -45/45 V, 0/90 H, and -45/45 H print protocols. A minimum of three samples were printed for each material and condition. While the cooling rates of the various materials tested undoubtedly have slightly different optimal print parameters, the tests were conducted using the same protocol to ensure that the only variable being compared be the weight percent loading of stainless steel in the ABS-SS.

With the final protocol for the 0/90 V and -45/45 V prints determined, (the latter being exactly the same as the former, just with a 45° rotation of the infill), 0/90 H single bar prints were built and tested, and when observing that the interlayer diffusion also appeared to be low, travel time was decreased to the maximum that the Hyrel System 30M could manage while still maintaining dimensional accuracy. With the final protocols for 0/90 V, -45/45 V, 0/90 H, and -45/45 H bars determined, and baseline tests performed for all of these orientations for pure ABS, the stage was set for PMC tests.

3.4 Materials Characterization and Testing

3.4.1 Tensile Testing

All test specimens were labeled before testing. An example of a properly labeled set of -45/45 H tensile bars are shown in Figure 13a. Two black lines were marked within the center of the bar to represent the gage length. Because a successful test was characterized by the location of the fracture in the gage length of the test specimen, the labeling of the tensile bar was a means of clarification on whether the test passed or failed. If a bar was considered a failed test its data were not used for analysis. An example of a passing test can be seen in Figure 13b.

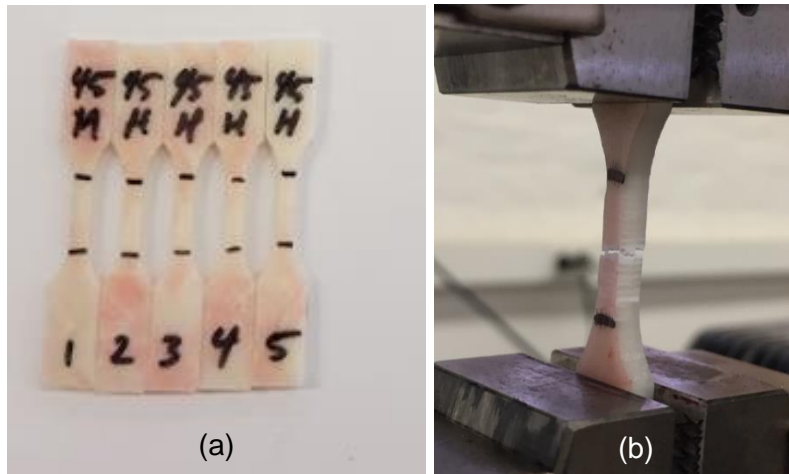


Figure 13: A labeled set of white ABS -45/45 H tensile testing bars (a) and the results of a tensile bar passing a tensile test with a fracture within the specified gage length (b).

The center of each individual bar was measured for its thickness, width, and length. These data were entered into the BlueHill 3 program that runs the test and collects data. The bars were then secured in the Instron machine pneumatic clamps equally on either side of the gage length. Once secured, the bars were pulled with the Instron 5567A, as seen in Figure 14, and the BlueHill 3 program recorded data received from the Instron. The strain rate for all tensile tests was 1mm/min. The tensile testing was completed until there were at least three successful tests in each print case. All variations of the composite samples were tested on the Instron Machine and the average tensile strength of the samples became a data point with a standard deviation for that specimen. All of the data points were saved in a spreadsheet. The data from the tests were used to find ultimate tensile strength (UTS), maximum load, and maximum strain. From the collected data, ductility, elastic modulus, and yield strength were determined.



Figure 14: The Instron 5567A was used for tensile testing.

3.4.2 Differential Scanning Calorimetry

Differential scanning calorimetry (DSC) was used to observe the various thermal properties of polymers. Through the use of DSC, the samples' heat capacity, heat flow, T_g , crystallization temperature, and melting temperature can be determined [17].

In order to complete a successful run of DSC, an empty reference pan and a sample pan were prepared. On average, each polymer sample weighed 11 mg. The twelve samples that were tested included samples from factory ABS and all variations of ABS-SS.

The DSC machine was calibrated so that each sample followed the same exact test parameters. The DSC used modulation at an amplitude of 0.5K. Each sample test would begin equilibrate at 30°C, and modulate at the rate of ± 0.50 °C/min. After remaining isothermal for 20 minutes, the sample was ramped to 250°C at the rate of 0.50 °C/min. The sample would equilibrate at 250°C, remain isothermal at this temperature for another 20 minutes, and then begin the cooling process. The samples cooled at a rate of 0.50 °C/min until it reached the starting temperature of 30°C. When the sample equilibrated at the final temperature, the testing was complete. Each run of this test took about 15 hours.

The recorded data from DSC provided valuable information about the thermal behaviors of the tested materials. DSC calculated the heat capacity, ΔC_p , of the materials with units of J/(g·K). The T_{min} and T_{max} are also identified in order to create a sinusoidal curve that approximates the T_g .

3.4.3 Dynamic Mechanical Analysis

The sample was loaded for dynamic mechanical analysis after the machine was calibrated. Sample length for all samples was 0.625 mm as determined by the separation of the grips. DMA was then conducted from -125°C to 120°C at 2 °C/min with a target amplitude of 1 μ m and a 1 Hz frequency. The resulting graphs were analyzed.

The results also provided data to calculate the C-factor. This number indicates how the fillers affect the composites by comparing the moduli in the glassy and rubbery regions of the graph. If the number is higher, this signifies that the filler is less effective. The equation to determine the C-factor is: $C = (E'_g / E'_r)_{composite} / (E'_g / E'_r)_{pure}$. E'_g and E'_r are the storage modulus values in the glassy region (90°C) and the rubbery region (120°C) respectively.

3.4.4 Scanning Electron Microscopy

After the samples underwent tensile testing, the fracture surface was observed with the scanning electron microscopy (SEM). The parts of the fracture surface that were imaged were as follows: the edge of the perimeter, only on the perimeter, the interface between the perimeter and the infill, only on the infill, and the interface of adjacent infill layers. SEM provided information about the type of fracture experienced and the effect of the metal particles on such fracture. The

corresponding micrographs for the samples were compared in terms of porosity, uniformity, and any gaps between layers. If there were no clear distinctions between layer boundaries and infill interfaces, micrographs were taken of the edge of the perimeter and any features on the surface. The micrographs were compared visually and the corresponding tensile data were compared. Conclusions were drawn about how the layer welding affected the fracture of each sample.

Chapter 4: Results and Discussion

4.1 Optical Microscopy of the Processed Composites

Optical micrographs were used as the first examination for homogeneity within ABS-SS composites. The edge and center of an ABS-SS23 batch were examined in order to verify homogeneity throughout the entire batch. Figure 15a shows the edge of a dried batch of ABS-SS23 at 5 \times magnification. It shows a uniform dispersion due to its consistent color. When the same sample was observed at its center at 20 \times magnification, the metal particles can be seen well dispersed and well coated in ABS throughout the material, as shown in Figure 15b.

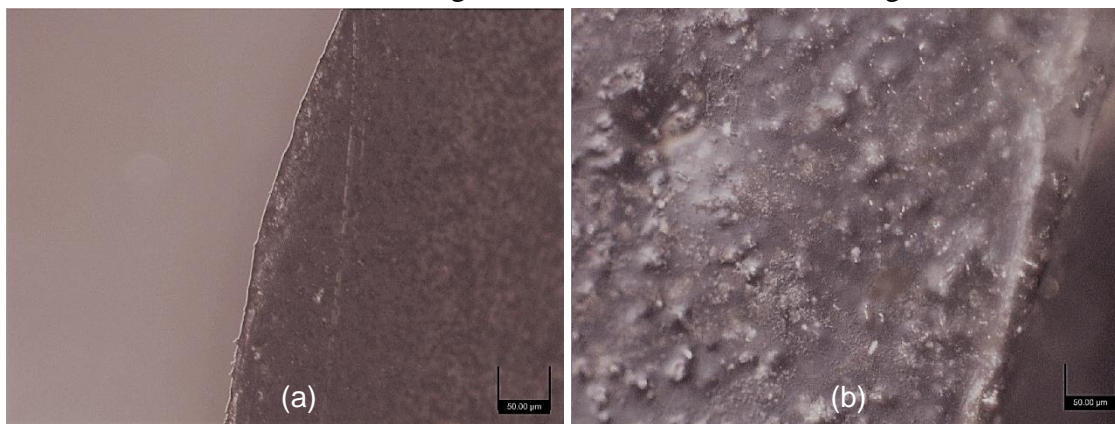


Figure 15: Edge of ABS-SS23 at 5 \times magnification (a), (b) center of a batch of ABS-SS23 at 20 \times magnification. The scale bars for both micrographs represents 50 μm .

Optical microscopy provided an initial confirmation of uniform particle dispersion within composite batches, however it was critical that homogeneity of the material was examined at every step of its processing. In order to do so, SEM was utilized to increase accuracy with higher magnifications, verify homogeneity, and examine layer adhesion of tensile bars.

4.2 Differential Scanning Calorimetry

A DSC analysis was performed to characterize the thermal behavior and properties of prepared polymers and polymer-metal composites in order to better understand the materials' structures and functionality. The first heating cycle from an ABS-SS23 DSC test was not used for analysis, as the samples contained trapped solvent that evaporated during the first run. The second and third heating cycles yielded uniform, repeatable, and reliable data that were used for analysis. Figure 16 shows the difference in thermal behavior between first and second heating cycle. The evaporation in the first heating corresponds to the boiling point of acetone, which is 56 $^{\circ}\text{C}$. The data from second and third heating runs were more consistent with common findings. The ABS-

SS23 composite exhibited T_g of 108.47°C , which surpassed the T_g of ABS of approximately 105°C .

Though the first heating run of ABS-SS23 was not reliable, its findings led to an alteration of the methodology in order to inhibit trapped acetone, as seen in Figure 16a. Vacuum ovens, hot plates, and robust drying procedures were put in place to reduce the amount of remaining solvent in composite batches and increase homogeneity within the composites.

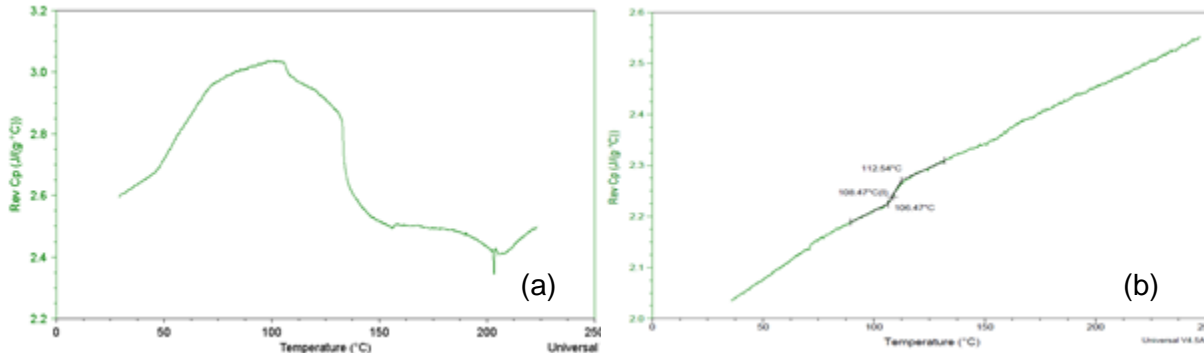
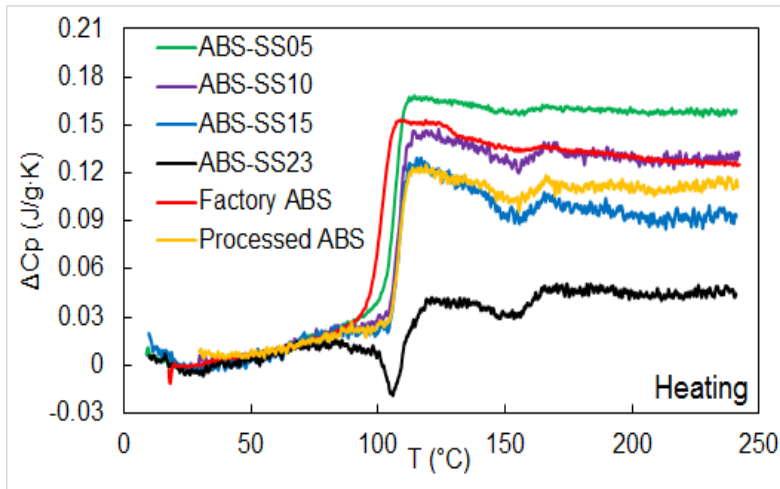
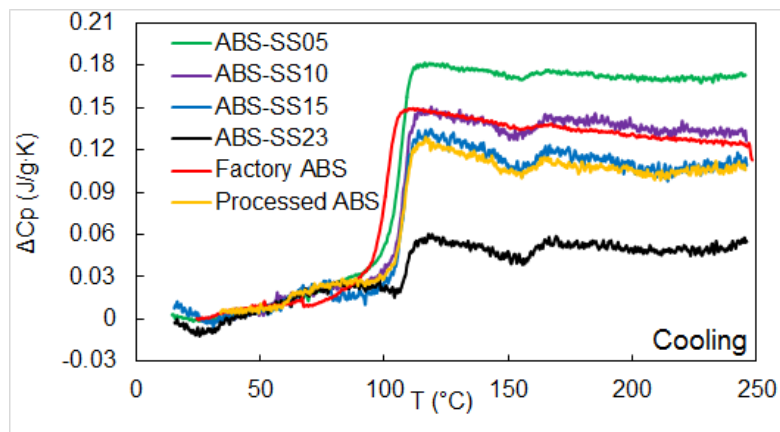


Figure 16: The graph of the first trial of ABS-SS23 (a) that shows non-uniformity caused by remaining acetone. The graph of the second trial of ABS-SS23 (b) which has a more uniform and reproducible pattern.

The DSC analysis presented the opportunity to examine the differences in heat capacity between ABS and SS-ABS composites. The thermal behavior of the ABS and ABS-SS composites during heating and cooling DSC cycles can be seen in Figure 17. During the heating phase of ABS-SS23, the material has a decrease in the shift of heat capacity (ΔC_p) by about $0.03 \text{ J}/(\text{g}\cdot\text{K})$ at 100°C preceding its glass transition and leveling off at $0.045 \text{ J}/(\text{g}\cdot\text{K})$. This behavior is due to the thermally conductive properties of 420 stainless steel. Increased SS powder loading decreased the heat capacity of the material after exceeding its T_g . This suggests that, although metal particles may not alter T_g dramatically, they do contribute to the heat capacity of the materials. The ABS-SS10 and 15 were the closest in behavior to the processed ABS.



(a)



(b)

Figure 17: Shows DSC heating (a) and cooling (b) cycle data from ABS and ABS-SS composites.

Figure 18 presents the T_g s of the different ABS and ABS-SS materials that were used in heating and cooling cycles of DSC. Through this figure, the difference between factory ABS and all other materials can be clearly seen. ABS-SS composites have T_g of 100-110°C as measured during heating cycles of DSC. The T_g of factory ABS is comparatively low at 101.65°C for heating. These data indicate that the various dyes and additives that were used in factory ABS altered its thermal properties. Additional DSC data are provided in Appendix B.

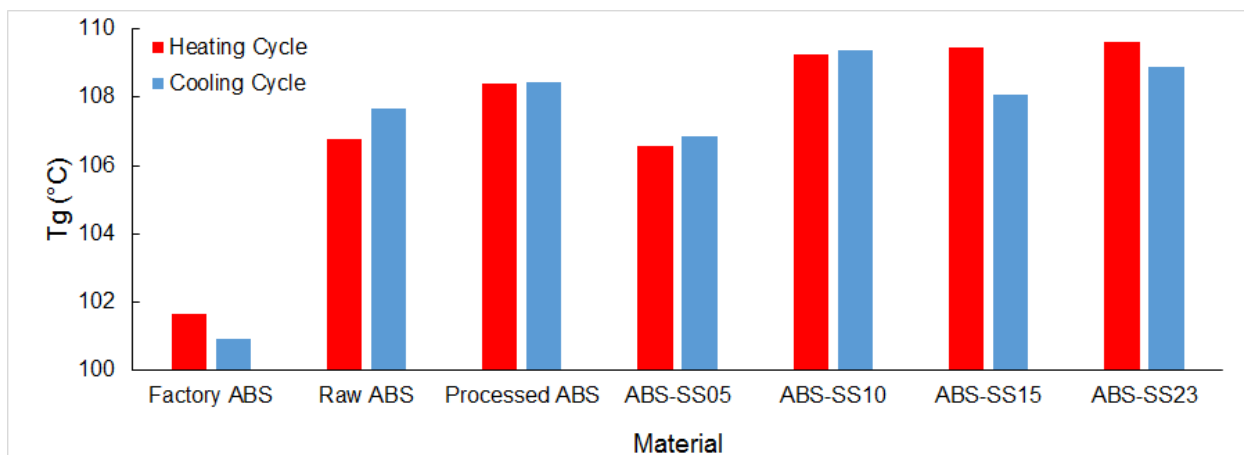


Figure 18: Shows DSC heating (red) and cooling (blue) cycle data from ABS and ABS-SS composites.

The results from DSC reaffirmed key points of this project. Because the ABS-SS composites yielded smooth glass transitions with a steady leveling off at various heat capacities, the samples represented homogeneous composites. This observation maintains the claim that uniform dispersion was achieved through the tested methodology. Because ABS-SS material was able to have similar thermal and mechanical properties to Processed ABS, the DSC testing demonstrated that polymer-metal composite materials can be made for more functionality due to metal particles without compromising tensile strength or thermal characteristics of the new material.

Though the focus of this project was on ABS, ABS-SS, and the behavior of ABS-SS with functionalized SS particles, the thermal behavior of nylon-6 was also observed. Appendix C shows the data of the heating and cooling cycles of raw nylon-6 pellets as well as vacuum dried nylon-6.

4.3 Extrusion

An extruder was used to create the spools of filament of a suitable diameter for the 3D printer. The distance between the spooler and extruder did not have a great effect on the diameter of the produced filament, but did have a great effect on the quality of the spooling process. Depending on the extrusion temperature and spooling speed, various distances between the spooler and the extruder were required to keep adequate tension in the filament. At proper tension, the filament would spool more neatly and the spooler speed gained more control over the filament diameter.

The extrusion temperatures varied for each material. The temperatures were picked in order to modulate the viscosity of the extruded filament. The ABS-SS05 had the lowest extrusion temperature because of the extreme shift in T_g as seen from the DSC thermographs on the material. Printing of this material was not pursued because of its extreme variance in thermal properties from the other composites and raw ABS. The ABS-SS10, 15, and 23 extrusion temperatures were lower than the extrusion temperature of raw ABS. The SS particles contributed to higher thermal

conductivity in the material, which would lead to a lower operating temperature for the extrusion process. This can be seen in the DSC data collected above, where in Table 2 each ABS-SS composite of increasing SS concentration had a lower shift in heat capacity after its T_g .

Table 2: Extrusion Temperatures for Neat and Composite Materials

Material	Extrusion Temperature (°C)
Raw ABS	175
ABS-SS05	155
ABS-SS10	170
ABS-SS15	165
ABS-SS23	160

The ABS-SS filament was extruded at least twice in order to eliminate voids in the extruded materials. The raw ABS did not require a second pass through, suggesting that some void formation was due to the presence of residual acetone in prepared ABS-SS. Figure 19 shows micrographs from the extrusion of ABS-SS23. Figure 19a is the cross-section of the extruded filament after one pass through the extruder. Figure 19b is the same filament sent through the extruder a second time. The material was extruded more than twice in order to reach the optimum diameter requirements for printing the filament.

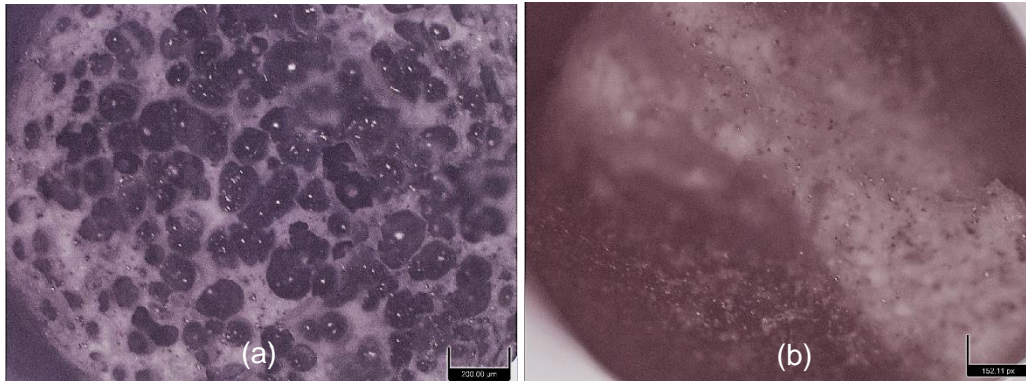


Figure 19: The micrograph (a) is the ABS-SS23 filament after one pass through the extruder. The micrograph (b) is the ABS-SS23 after a second pass through. The scale bars for both micrographs represents 200 μm .

The spooler speed was the variable with the greatest influence on the diameter of the filament. Spooler speed was increased to decrease the filament diameter; this was important for lower extrusion temperatures. If the spooler turned too fast, it would pull the filament out of the extruder, making it too thin. Likewise, a decrease in spooling speed was required to increase the

filament diameter at higher extrusion temperatures. If the spooler rotates slower, the filament would no longer be pulled as it is extruded, which increases the diameter. Unfortunately, this parameter had to be adjusted in an ad hoc fashion, which is a source of variability in the process.

4.4 Dynamic Mechanical Analysis

A DMA was performed on the extruded filament to study the viscoelastic behavior of the filament as a stress is applied. The temperature and frequency are varied and the results are summarized in Figure 20.

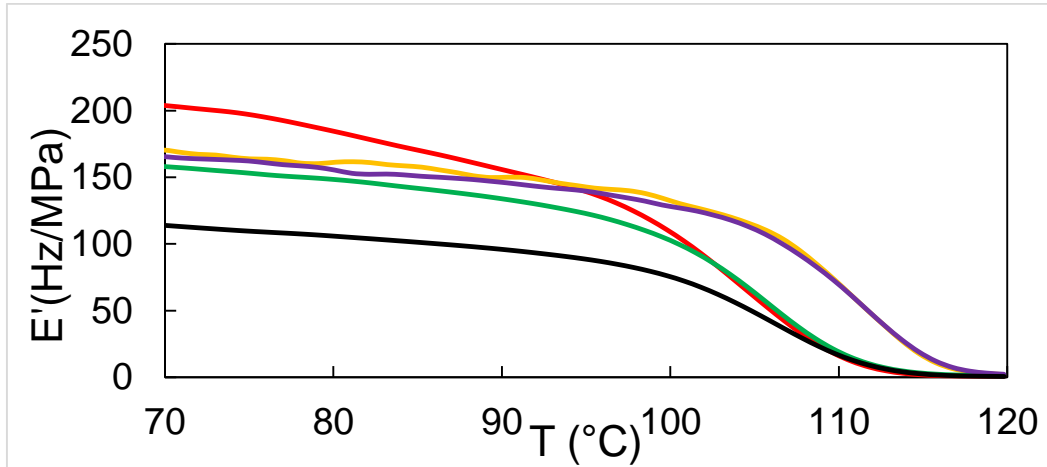


Figure 20: Dynamic mechanical analysis results showing the similar properties between the raw ABS and the ABS-SS10.

As the temperature increased, the storage modulus decreased. The raw ABS, the ABS-SS05, and the ABS-SS10 had very similar glassy E' values. The ABS-SS23 had the lowest E' value which indicates that it had the lowest stiffness out of all of the materials, while the factory ABS had the highest stiffness. T_g values based on the onset of E' decrease were determined. It is interesting to note that the raw ABS and the ABS-SS10 deviate from the factory ABS, ABS-SS05, and ABS-SS23. The T_g of raw ABS is 105°C. The material used as the "pure" material was the raw ABS. Table 3 contains the values for the C-factor.

Table 3: C-Factor values indicating the stiffness of the material in comparison to the raw ABS

Material	C-Factor
ABS-SS05	1.74
ABS-SS10	0.882
ABS-SS23	2.30
Factory ABS	2.37

The results from the calculation of the C-factor implicate that fillers in the factory ABS and the ABS-SS23 had the most negative impacts on the filament. They did not behave as the raw ABS did under stress. The ABS-SS10 had the lowest C-factor and therefore its fillers were the most effective in maintaining the properties of the material while also containing fillers compared to the other weight percentages of stainless steel.

4.5 Optimization of the Printing Process and Parameters

A thermal camera was used to view the heat flow and the relationships between the layers as they cool and as a new layer gets added. This camera assisted in understanding the thermal properties as the print was made. Based off of the results of the thermal camera, it is clear that the cooling rates and layer adhesion must be taken into consideration in order to obtain the best and most consistent tensile properties. Table 4 contains the values of print parameters that were determined through an optimization process. Print parameters were maintained for all materials. The horizontal and vertical prints have different cooling times, so different maximum fan speeds were used.

Table 4: Optimized printing parameters for both ABS and ABS-SS, the only thing altered being the maximum fan speed for horizontal prints and vertical prints

Print Temperature	Layer Thickness	Bead Width	Fill Density	Printing Speed	Max Fan Speed	Bed Temperature	Nozzle Diameter
237°C	0.2 mm	0.4 mm	100%	12.5 mm/s	<u>Vertical:</u> 68.75% <u>Horizontal:</u> 5%	90°C	0.35 mm

The number of bars printed at one time was also taken into consideration. This was pursued in order to ensure that the bars are printed efficiently and have consistent properties. Five-bar prints were compared to single-bar prints. It was determined that single-bar prints yielded the most consistent mechanical properties and therefore they were the bars used for the remainder of the testing.

For the optimization of horizontal bars, there must be a balance between the layer welding and the dimensional accuracy. Due to testing, the temperature of 237°C allowed for proper thermal behavior within the bead of filament. One of the parameters that was changed was the travel time. It is important to determine the proper travel time for each layer to cool enough so the next layer will not alter it, but also have each layer hot enough for the best layer adhesion. The best print speed was determined by increasing the print speed until the dimensions became inaccurate and was determined to be 12.5 mm/s.

Fan speed was the other printing parameter that was optimized. This was established by printing bars of the same orientation with a specified fan speed and repeating the process until the bars with the best tensile properties are determined. The fan speed for horizontal bars that lead to the best tensile properties was 5%.

For the optimization of vertical bars, the process for determining the best balance between layer welding and dimensional accuracy was slightly different. Since the vertical bars are built where the gage is printed along the cross section, the cooling rates had to be observed carefully. A skirt was built around each bar in order to allow the previously build layer to cool to the right temperature before the next layer was added. This led to increased tensile properties compared to the five-bar print. An indication as to why this was the case revealed itself by a visual inspection of the fracture surfaces, where the clear raster pattern visible on the bars with the macro suggested that there was not as much interlayer diffusion as there was in the bars where the macro was not applied and the skirt was built right around the bar, which had fracture surfaces showing no clear raster pattern. These observations suggested that the close proximity of the print head to the bar resulted in increased temperatures which facilitated interlayer diffusion which in turn increased the tensile strength of the bar.

The introduction of this macro resulted in single bar 0/90 V prints that took the same amount of time to print as 0/90 V five bar prints, yet used only 1/5 of the required filament, and the total elapsed print time for a 0/90 V bar was reduced to 53:00 minutes, where the bar was still dimensionally accurate, and offered tensile properties comparable to the higher recorded values in the literature.

4.6 Tensile Properties and Optimization

Tensile testing was performed to understand the mechanical properties of the materials such as UTS, yield strength, Young's modulus, and ductility. UTS and percent elongation were read directly from the stress-strain curves. Yield strength was calculated using the 0.2% offset method. The elastic modulus was calculated from the slope of the linear portion of the graph (elastic region). A representation of a typical stress-strain curve can be seen in Figure 21.

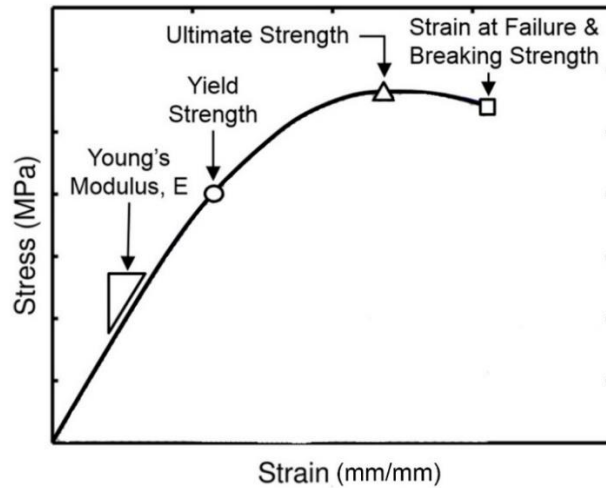


Figure 21: Representation of where each value of a mechanical property was collected from [10].

The first composite mixture that was made was called “batch 1,” “batch 2” was the second, etc. Tensile testing of the initial batches was used to determine the proper parameters for optimization. Figure 22 shows a comparison of the stress-strain curves from different batches in the generally weaker print orientation (0/90 V prints) of factory ABS. These are shown from batches 1 through 4, with 4 being the most recent and used for the final data analysis and comparisons throughout the rest of the results section. This justifies our printing and extrusion procedures and establishes that our data received from the tensile test were reproducible and accurate.

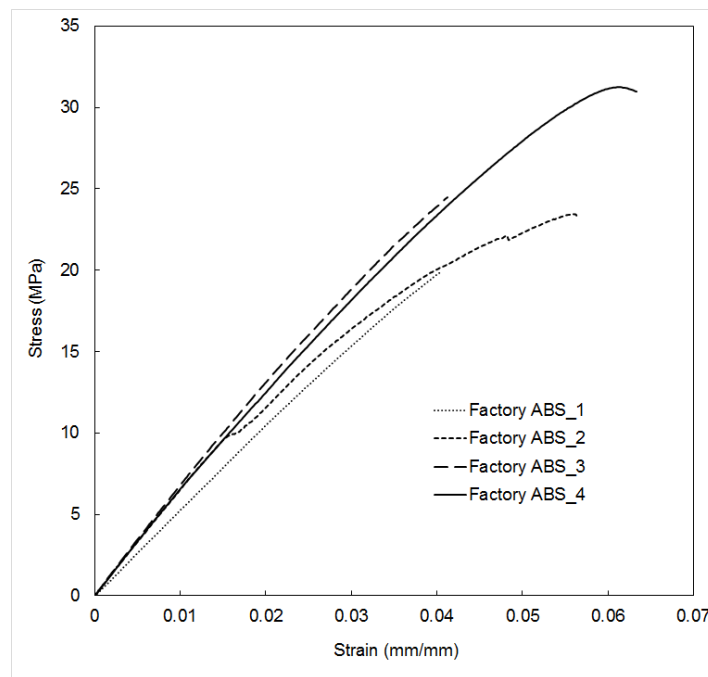


Figure 22: A comparison between batches 1 through 4 to assist in the optimization process of the printing parameters.

The 0/90 V prints of each material are compared in Figure 23. It is shown that ABS-SS10 and ABS-SS15 have similar mechanical behaviors to the factory ABS and raw ABS prints. The optimized g-code and print processes increased the properties of the single bar prints compared to literature values. The 0/90 V prints of raw ABS had an increase in UTS of ~40% compared to the average of values collected from authors Cantrell and Riddick [10, 11]. The 0/90 H prints of raw ABS increased in UTS by ~23% compared to average values collected by Cantrell et al [10]. The -45/45 V prints of raw ABS exhibited ~29% higher UTS values compared to values found by Cantrell and Riddick [10, 11]. The -45/45 H prints of raw ABS increased in UTS by ~39% compared to data collected by Cantrell, Riddick, and Ziemian [10, 11, 14].

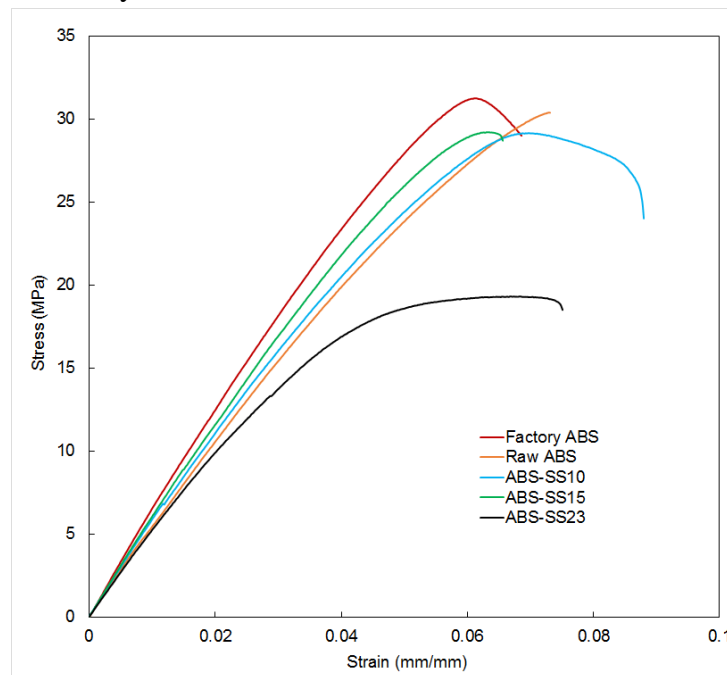


Figure 23: A comparison between the best tensile tests of the 0/90 V orientation in all compositions.

Figure 24 contains the data that show that UTS is relatively unaffected by a SS concentration of 10 wt% to 15 wt% in the raw ABS matrix. The decrease in UTS experienced in 10, 15, and 23 wt% builds of the 0/90 vertical orientation are on average ~4%, ~4%, and ~40% respectively. This is contradictory to the test results found in the literature, where in, any amount of SS in the ABS matrix was detrimental to the overall mechanical properties [13, 16]. The 0/90 V prints of the ABS-SS23 composite had an average UTS that was ~40% greater than the UTS of the injection molded ABS 20% iron-reinforced composite bars tested by Sa'ude [16]. The 0/90 V prints of the ABS-SS10 composite showed an average UTS ~37% greater than that of the vertical ABS 5% TiO₂ reinforced composite prints tested by Perez [13]. It was observed that somewhere between 15 wt% SS and 23 wt% SS is an inflection point at which the SS in the raw ABS matrix starts to affect the mechanical properties negatively.

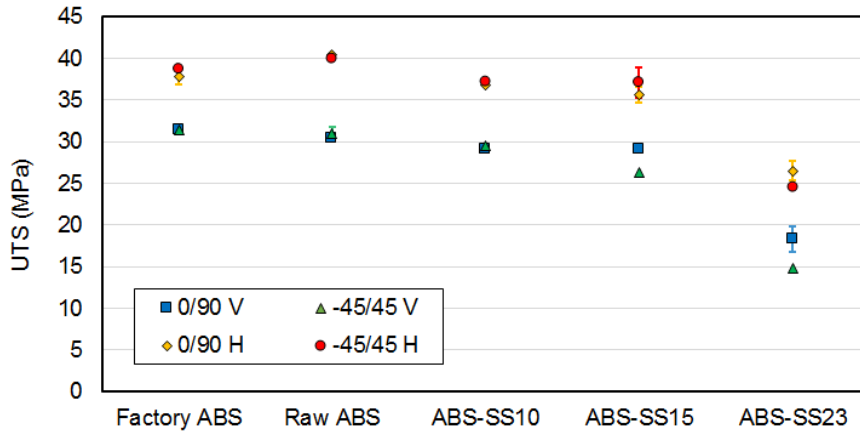


Figure 24: The UTS values collected for each print orientation and material composition.

The vertically oriented bars experienced on average of ~76% less elongation compared to the horizontal print orientations, as seen in Figure 25. This can be attributed to the fact that vertically printed bars are subjected to a force normal to the printed layer plane during tensile testing, whereas, in horizontally printed bars the forces applied during testing are parallel to the print plane. Ductility was found to increase with SS content in vertical print orientations. The vertical prints of ABS-SS (both -45/45 V and 0/90 V) exhibited, on average, values in ductility ~14% higher than recorded for the raw ABS vertical prints.

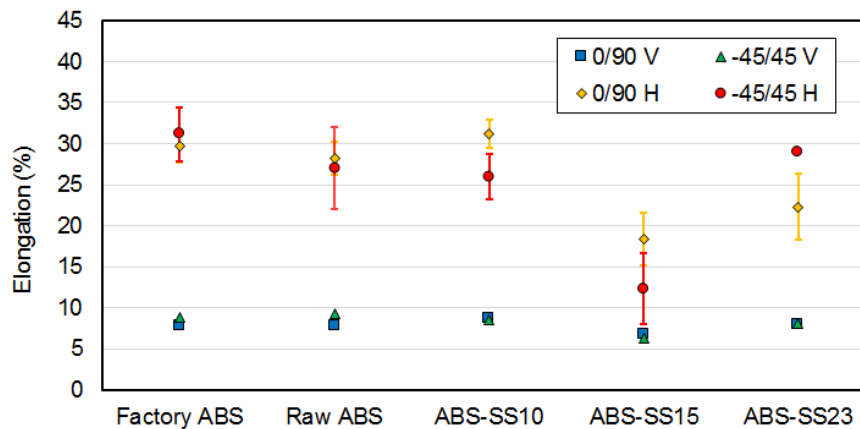


Figure 25: The percentage elongation (ductility) values collected for each print orientation and material composition.

Figure 26 shows how ABS-SS composites of SS concentrations 10 and 15 wt% showed an approximately 10% increase in elastic modulus compared to the raw ABS prints. The ABS-SS23 had a decrease of approximately 10% in elastic modulus compared to the raw ABS prints; again showing a potential for an effective inflection point where the SS concentration in ABS starts to drastically decrease original properties. On average for horizontal and vertical prints of ABS-SS10 the Young's modulus increased by an average of ~5% compared to the raw ABS prints. For vertical

and horizontal prints of ABS-SS15, the elastic modulus increased by an average of 6.1% compared to the raw ABS prints. The vertical and horizontal ABS-SS23 prints experienced an average decrease in elastic modulus of ~12% compared to the raw ABS prints.

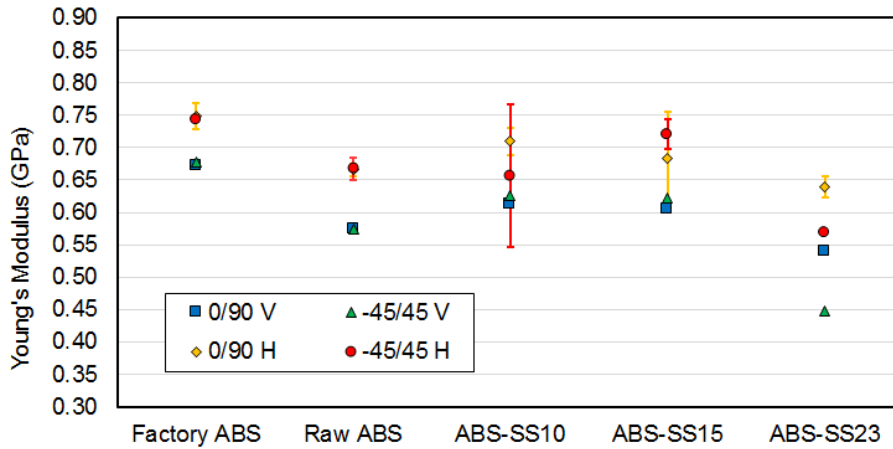


Figure 26: The Young's modulus values collected for each print orientation and material composition.

4.7 Fractography Using Scanning Electron Microscopy (SEM)

Scanning electron microscopy (SEM) was utilized to observe material characteristics and interlayer bonding on the fracture surface of the tensile testing bars. All SEM samples that were taken from vertical bars were from the bottom portion of the printed tensile bar. A visual representation of this can be seen in Figure 27.

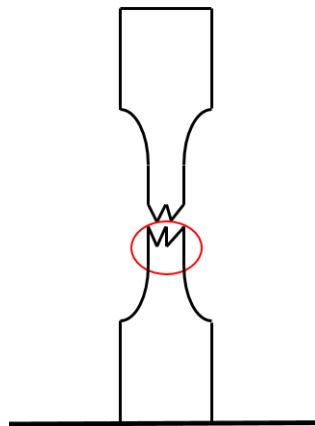


Figure 27: The red circle indicates where SEM samples were taken when taken from vertical bars when taken off of the print bed. The line on the bottom represents the print bed.

The image in Figures 28 (a,b) indicate that there is evidence of the stainless steel particles pinning the distribution and advance of the damage. This has been inferred from the elongated traces left by the particles on the fracture surfaces, whose directions coincide with the layer

deposition directions. This conclusion becomes obvious from the appearance of the fracture surfaces that span consecutive layers deposited in different directions, leading to traces elongated in the same respective directions. Despite poor wetting to the polymer matrix, the presence of the stainless steel particle additives clearly impacted the advance of damage, and further improvements can be achieved by increasing the adhesion of the particle additions to the polymer matrix. Also, triangular patterns in between print layers was observed using SEM. These triangles can be found in Figures 28 (e,f) at different magnifications. These gaps are a representation of spaces in between the circular beads of filament that are printed into samples.

In Figure 31(c,d), fractographic images of a -45/45 V ABS-SS15 print, indicate that there was incomplete layer diffusion resulting in two distinct fracture patterns. The dark region of the image represents layer delamination where a low ductility fracture pattern can be observed, as compared to the lighter region, where the increased deformation of the surface indicates a more ductile fracture rather than an abrupt, brittle fracture due to layer delamination.

The interlayer bonding within a sample was critical because it would help determine why samples broke at the tensile load that they did as well as further investigate the relationship between tensile strength and build orientation. Filament that was too thin as well as poor interlayer bonding led to lower tensile data and brittle fractures, as seen in Figures 31 (e,f).

The porosity of ABS-SS composites can be seen in Figure 32. The magnified micrographs display porosity in ABS-SS samples. Figures 32 (a,b) also depict striations. These markings follow the direction in which the sample's layer was printed. This implies that the gaps are a result of print direction and potential filament porosity.

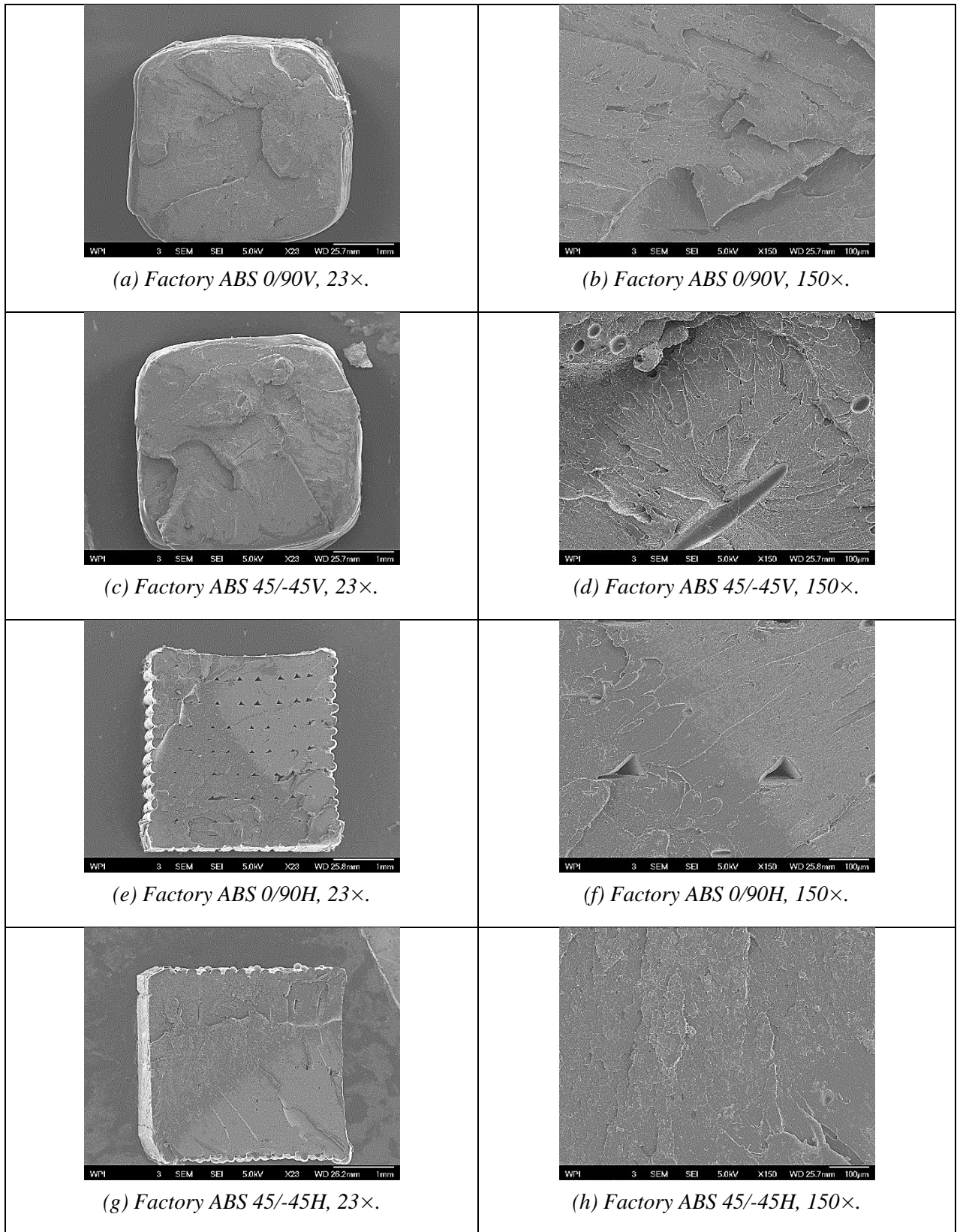


Figure 28. SEM images of Factory ABS fracture surfaces at low (a,c,e,g) and high (b,d,f,h) magnification.

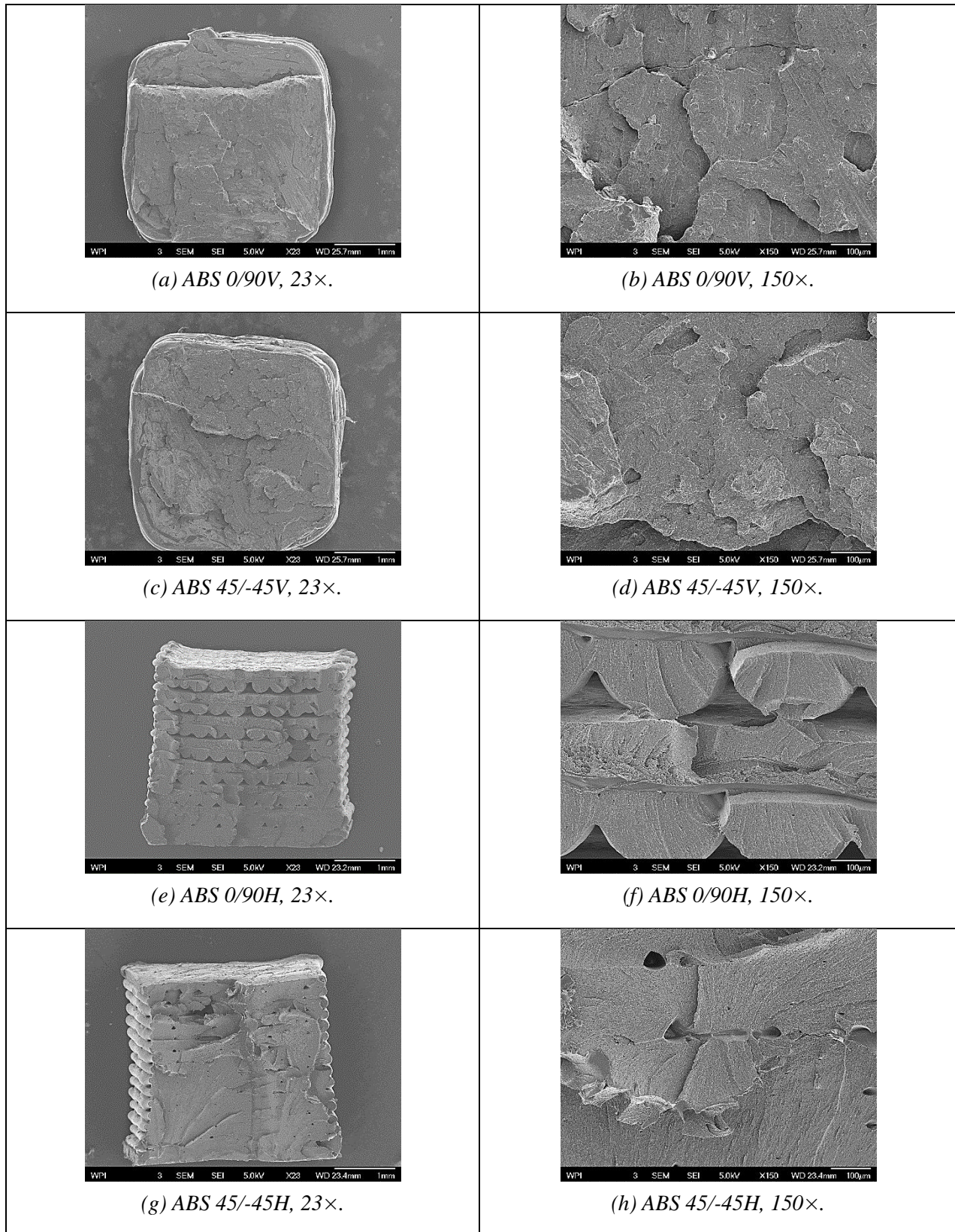


Figure 29. SEM images of ABS fracture surfaces at low (a,c,e,g) and high (b,d,f,h) magnification.

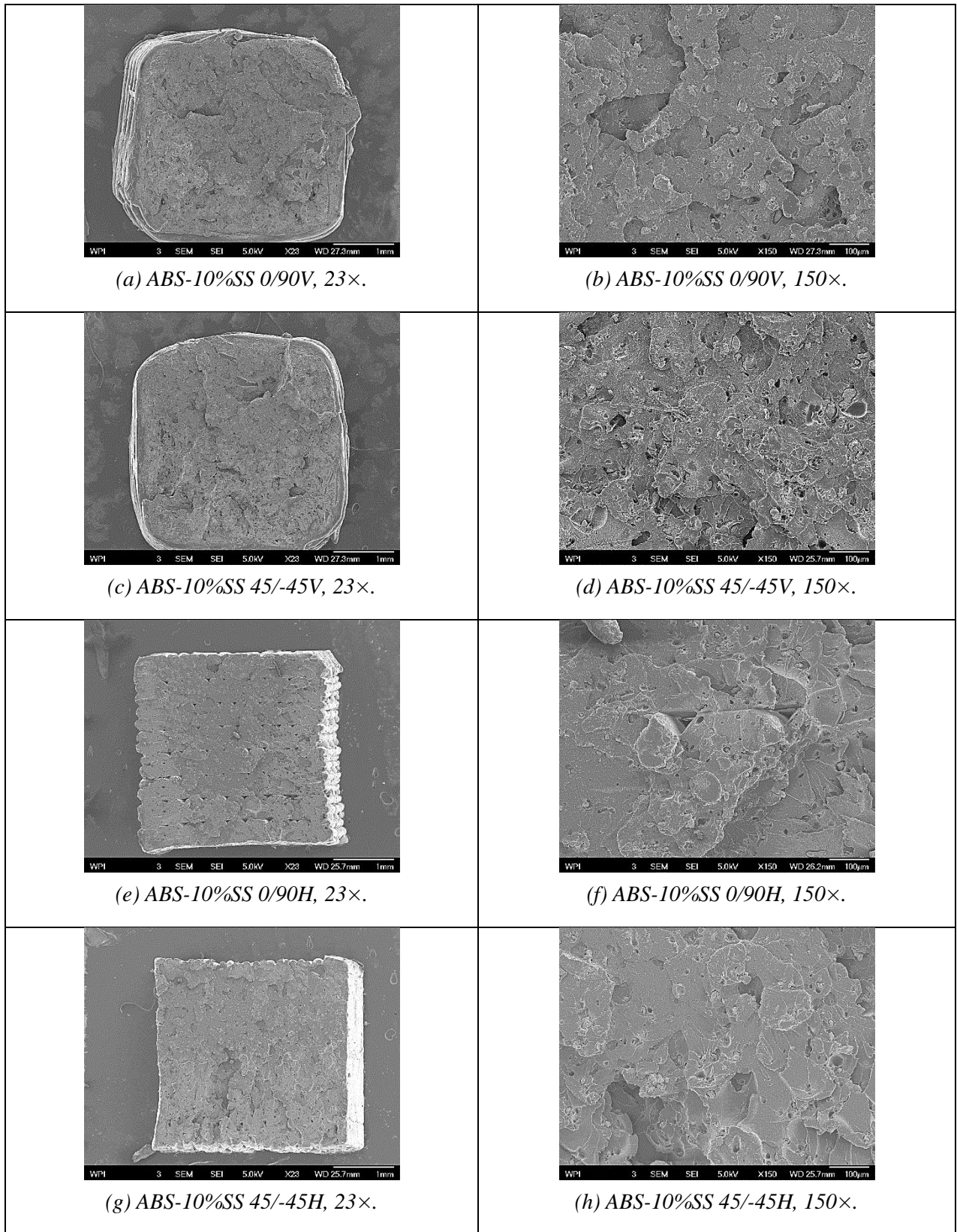


Figure 30. SEM images of ABS-10%SS fracture surfaces at low (a,c,e,g) and high (b,d,f,h) magnification.

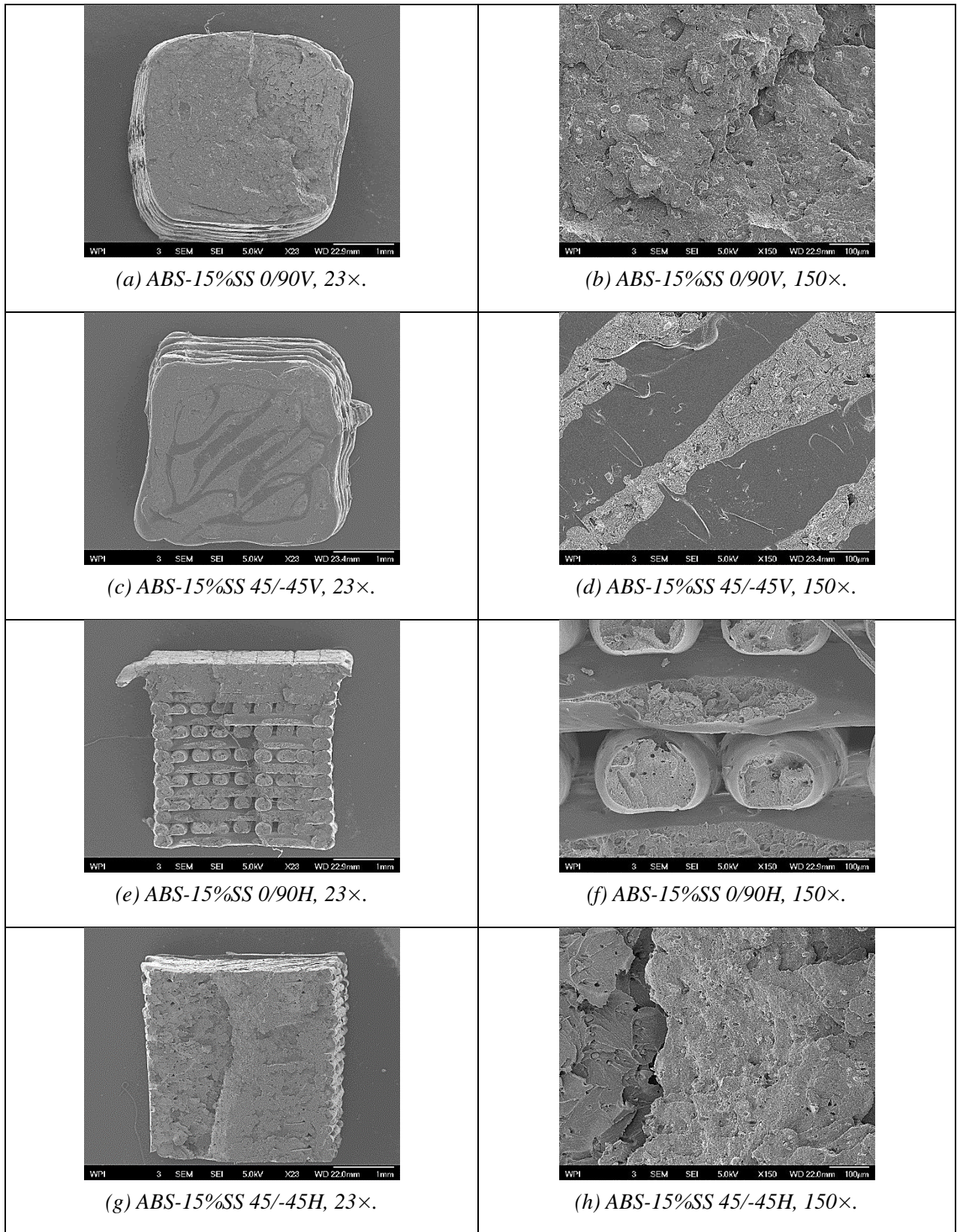


Figure 31. SEM images of ABS-15%SS fracture surfaces at low (a,c,e,g) and high (b,d,f,h) magnification.

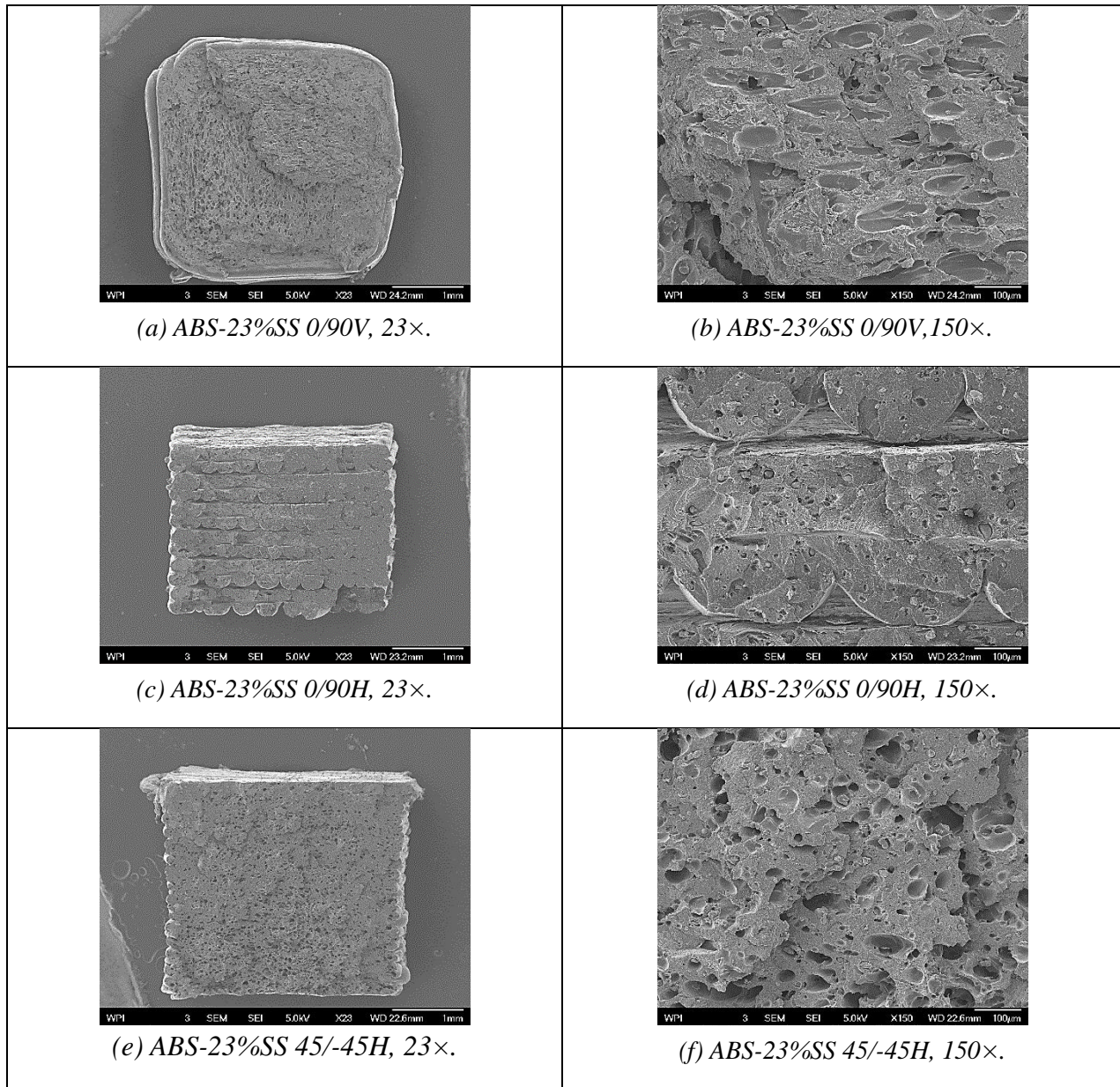


Figure 32. SEM images of ABS-23%SS fracture surfaces at low (a,c,e,g) and high (b,d,f,h) magnification.

The ABS-SS samples that underwent SEM had hackle markings along the fracture surface. Hackle markings are morphologies that indicate small cracks along the fracture surface [18]. An example of what hackle markings look like on the SEM micrographs can be seen in Figure 33. These hackle markings appear throughout the surface of the samples, which shows that failure of the tensile specimens does not occur only on the edges of the bar. Failure occurs across the entire layer between the polymer. The hackle markings also occur near the metal particles. These metal particles have voids surrounding them, indicating that though the metal particles were uniformly dispersed, there was weak adhesion between the metal particles and the plastic. This weak adhesion caused crack propagation along the layer.

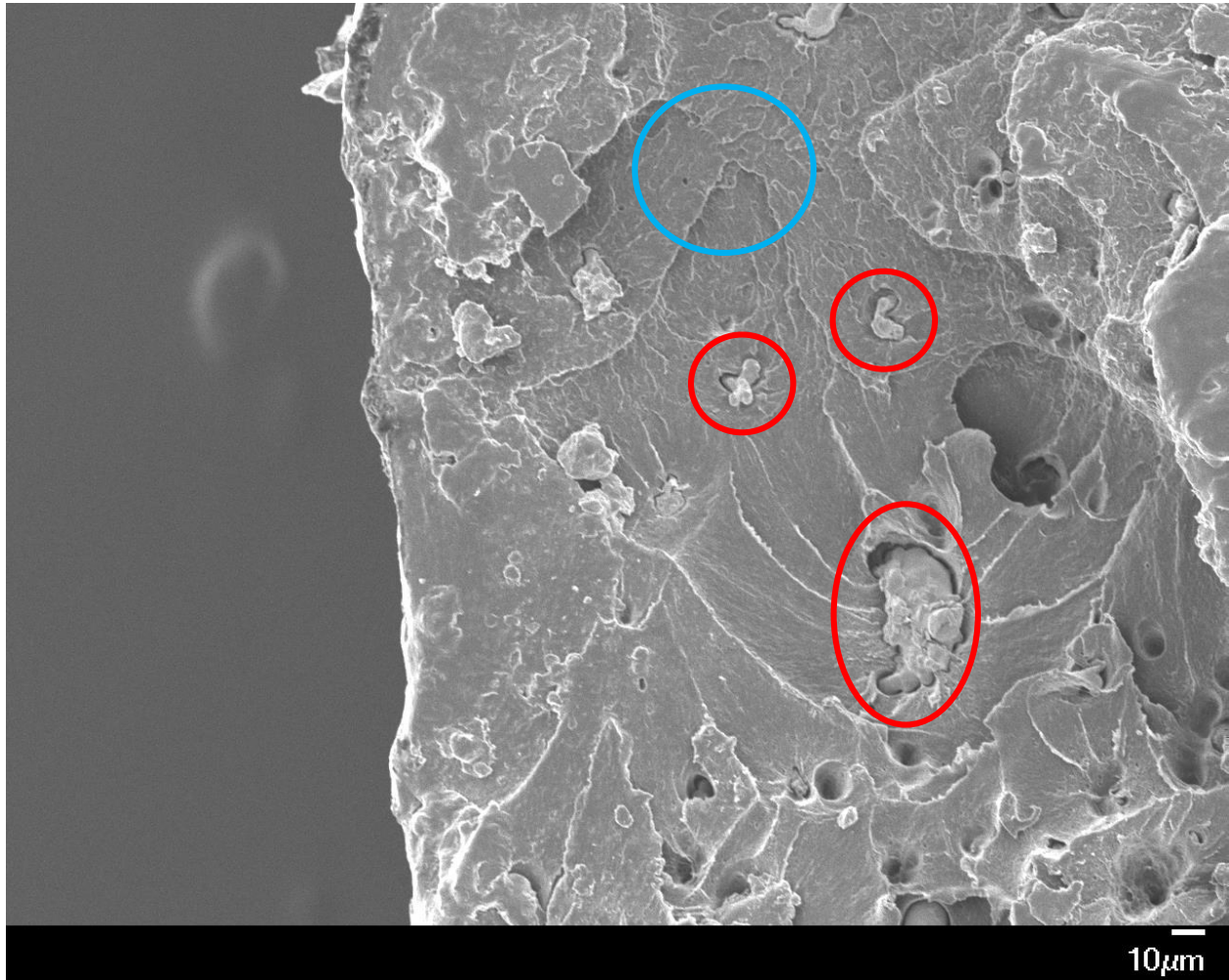


Figure 33: Micrograph of ABS-SS10 -45/45 H at 330 \times magnification distinctly shows the particles within the polymer matrix. Some of the metal particles are presented in the red circles. Hackle markings are shown within the blue circle.

Additional SEM were collected for further investigation. To investigate interlayer bonding and levels of porosity, SEM samples were also cut in half. Their cross sections were observed. These cross sections showed significant interlayer cohesion. This observation had a major impact in proving the printing parameters that were chosen as ideal. An SEM sample showing interlayer cohesion can be seen in Figure 34.

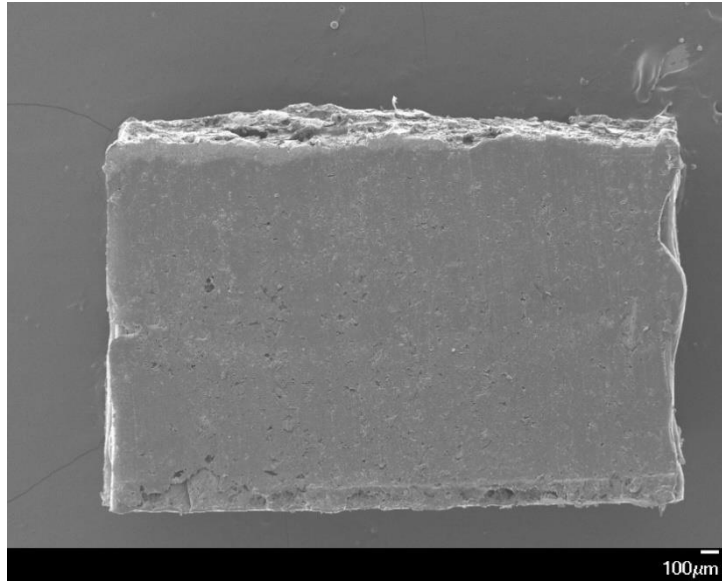


Figure 34: Micrograph of cross section of ABS-SS10 -45/45 H SEM sample.

An ABS-SS10 -45/45 V sample had unexpected SEM results; The sample did not show any distinct pattern that is common with other bar fractures with a -45/45 build orientation. Through Figure 36, it is observed that the patterns between the two ABS-SS10 -45/45 V bars have different textures. More investigation and observation of their individual tensile results show a reason behind the different properties. Vertical bar 1 had higher tensile strength than vertical bar 2. Vertical bar 1 had a more ductile tensile test result while vertical bar 2 had a brittle fracture. This can be seen through the data in the graphs of Figure 35. The SEM samples and tensile results show that the vertical bar 1 had a different texture and higher tensile results that vertical bar 2 due to stronger layer cohesion. The cross section of these SEM samples were also observed. A direct picture comparison can be found in Figure 36.

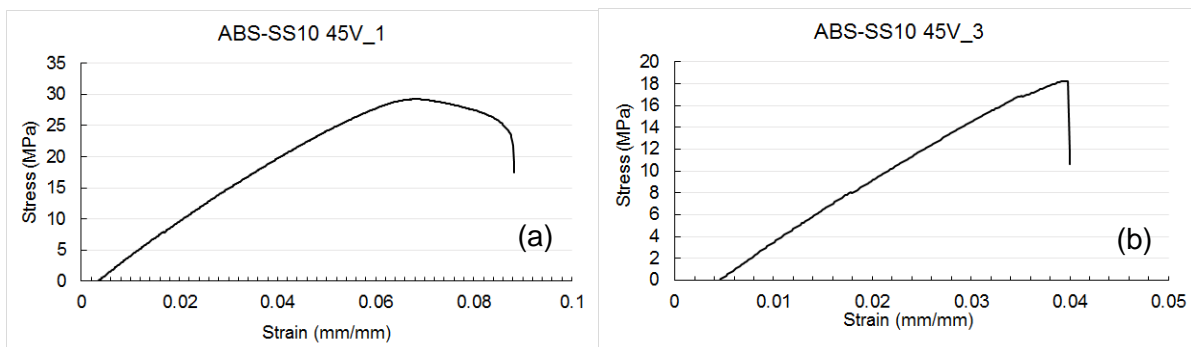


Figure 35: The tensile results of ABS-SS10 -45/45 V bar 1 (a) and 2 (b).

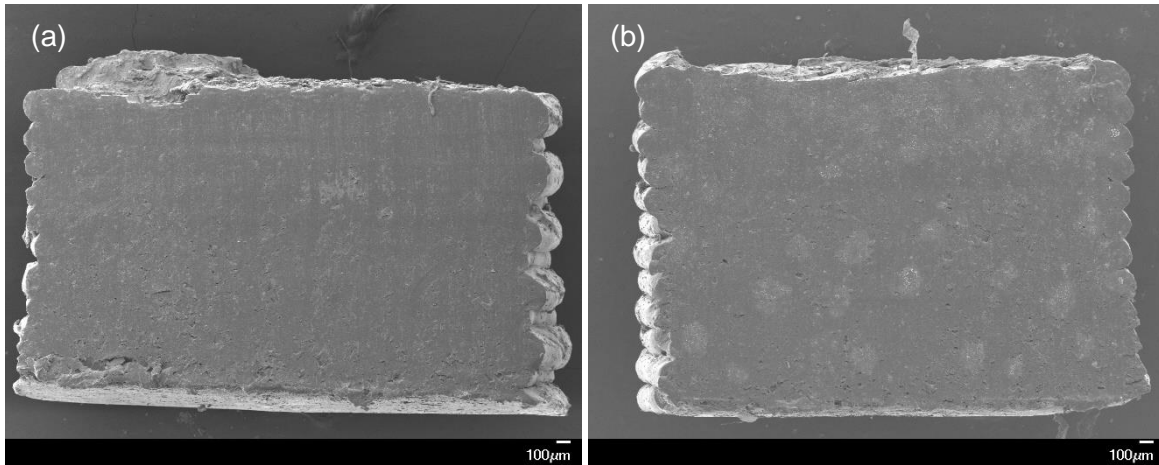


Figure 36: Micrographs of cross sections of ABS-SS10 -45/45 V bar 1 (a) and 2 (b).

4.8 Added Functionality of Polymer-Metal Composites

ABS-SS10 and ABS-SS15 had mechanical properties very similar to the neat ABS prints but with added functionalities intrinsic to the ferrous stainless steel powder added to the ABS-SS materials. The SS powder did not increase the electrical conductivity of the composite materials; however, the SS powder added magnetic properties to the composite prints.

Conclusions

By establishing an optimized methodology to successfully produce polymer-metal composites and filaments compatible with 3D printing, tensile bars were produced with high dimensional accuracy, strong interlayer diffusion, and good tensile properties. For raw ABS in 0/90 H orientation, the tensile bars obtained an average UTS equal to 40.4 MPa and an average elongation % equal to 28.4%. For the same configuration of ABS-SS10, the UTS was equal to 36.7 MPa and the elongation % was equal to 27.5%. The ABS-SS with 10 wt% loading preserved and improved the mechanical and thermal properties of raw ABS more than the other weight percentages. Added functionality, magnetism, was achieved of the new polymer-metal composites.

Moreover, the results of this project present more directions for research within fused filament fabrication (FFF) composite fabrication. There is a potential for FFF composite material with enhanced mechanical properties as well as increased electrical and thermal conductivity. Supplemental functionalities can be pursued not only through using new base polymers such as semi-crystalline nylon-6, but it can also be explored through additives such as shape memory alloys, titanium, and nickel.

Bibliography

- [1] M. Nikzad, S. H. Masood, and I. Sbarski, "Thermo-mechanical properties of a highly filled polymeric composites for Fused Deposition Modeling," Swinburne University of Technology, 2011.
- [2] K. V. Wong and A. Hernandez, "A Review of Additive Manufacturing," Department of Mechanical and Aerospace Engineering, University of Miami, International Scholarly Research Network, vol. 2012.
- [3] Reprap.org, Content is available under GNU Free Documentation License 1.2.
- [4] S. Kumar and J. P. Kruth, "Composites by rapid prototyping technology," ed: Elsevier Ltd., 2009.
- [5] S. Kalpakjian, I. I. Of technology, and S. R. Schmid, *Manufacturing Engineering and Technology 7th Edition*, 7th ed. Singapore, Singapore: Pearson Education South Asia, 2013.
- [6] J. F. Rodriguez, J. P. Thomas, and J. E. Renaud, ""Mechanical behavior of acrylonitrile butadiene styrene (ABS) fused deposition materials. Experimental investigation," vol. 7, ed: Emerald Insight, 2001.
- [7] L. Li, Q. Sun, C. Bellehumeur, and P. Gu, "Investigation of Bond Formation in FDM Process," *Journal of Manufacturing Processes*.
- [8] F. Rayegani and G. C. Onwubolu, "Fused deposition modelling (FDM) process parameter prediction and optimization using group method for data handling (GMDH) and differential evolution (DE)," vol. 73, ed. The International Journal of Advanced Manufacturing Technology, 2014, pp. 509-519.
- [9] I. Durgun and R. Ertan, "Experimental investigation of FDM process for improvement of mechanical properties and production cost," vol. 20, ed. Rapid Prototyping Journal Emerald Group Publishing Limited, 2013, pp. 228-235.
- [10] J. Cantrell, S. Rohde, D. Damiani, R. Gurnani, L. Di Sandro, J. Anton, A. Young, A. Jerez, D. Steinbach, C. Kroese and P. Ifju. Experimental characterization of the mechanical properties of 3D printed ABS and polycarbonate parts. 2017, DOI: 10.1007/978-3-319-41600-7_11.
- [11] J. C. Riddick et al., "Fractographic analysis of tensile failure of acrylonitrile-butadiene-styrene fabricated by fused deposition modeling," *Additive Manufacturing*, vol. 11, pp. 49-59, Jul. 2016.
- [12] A. R. Torrado and D. A. Roberson, "Failure Analysis and Anisotropy Evaluation of 3D-Printed Tensile Test Specimens of Different Geometries and Print Raster Patterns," vol. 16, ed. *Journal of Failure Analysis and Prevention: ASM International* 2016, 2016, pp. 154-164.
- [13] A. R. Torrado Perez, D. A. Roberson, and R. B. Wicker, "Erratum to: Fracture surface analysis of 3D-Printed tensile specimens of novel ABS-Based materials," *Journal of Failure Analysis and Prevention*, vol. 14, no. 4, pp. 549–549, Jul. 2014.
- [14] Ziemian et al., "Tensile and fatifue behavior of layered acrylonitrile butadiene styrene," *Rapid Prototyping Journal*, vol. 21, no. 3, pp. 270-278, Sep. 2013.

- [15] K. Chockalingam et al., "Enhancement of Anisotropic Strength of Fused Deposited ABS Parts by Genetic Algorithm," *Materials and Manufacturing Processes*, vol. 31, no. 15, pp. 2001-2010, Dec. 2016.
- [16] N. Sa'ude, M. S. Wahab, and M. H. I. Ibrahim, "Effect of Powder Loading and Binder Materials on Mechanical Properties in Iron-ABS Injection Molding Process," *Applied Mechanics and Materials*, vol. 315, pp. 532–586, Sep. 2016. [Online]. Available: <https://www.researchgate.net/publication/237005209>. Accessed: Jan. 30, 2017.
- [17] Humboldt University of Berlin, "Investigation of Polymers with Differential Scanning Calorimetry," 2015.
- [18] Brown, Eric N., Scott R. White, and Nancy R. Sottos. "Microcapsule induced toughening in a self-healing polymer composite." *Journal of Materials Science* 39.5 (2004): pp. 1703-1710.
- [19] G. W. Melenka, B. K. O. Cheung, J. S. Schofield, M. R. Dawson, and J. P. Carey, "Evaluation and prediction of the tensile properties of continuous fiber-reinforced 3D printed structures," *Composite Structures*, vol. 153, pp. 866–875, Oct. 2016.
- [20] M. V. Jose *et al.*, "Morphology and mechanical properties of nylon 6/MWNT nanofibers," *Polymer*, vol. 48, no. 4, pp. 1096–1104, Feb. 2007.
- [21] K. S. Boparai, R. Singh, and H. Singh, "Process optimization of single screw extruder for development of nylon 6-Al-Al₂O₃ alternative FDM filament," *Rapid Prototyping Journal*, vol. 22, no. 4, pp. 766–776, Jun. 2016.
- [22] A. W. Fatimatuzahraa, B. Farahaina, and W. A. Y. Yusoff, "The effect of employing different raster orientations on the mechanical properties and microstructure of Fused Deposition Modeling parts," ed: 2011 IEEE Symposium on Business, Engineering and Industrial Applications (ISBEIA), Langkawi, Malaysia, 2011.
- [23] A. Garg, A. Bhattacharya, and A. Batish, "Chemical vapor treatment of ABS parts built by FDM: Analysis of surface finish and mechanical strength," ed. *The International Journal of Advanced Manufacturing Technology: Springer-Verlag London* 2016, 2016, pp. 1-17.
- [24] M. Kaveh, M. Badrossamay, E. Foroozmehr, and A. H. Etefagh, "Optimization of the printing parameters affecting dimensional accuracy and internal cavity for HIPS material used in fused deposition modeling processes," vol. 226, ed, 2015, pp. 280-286.
- [25] L. Li, Q. Sun, C. Bellehumeur, and P. Gu, "Investigation of Bond Formation in FDM Process," ed: *Journal of Manufacturing Processes*.
- [26] M. Montero, S. Roundy, D. Odell, S.-H. Ahn, and P. K. Wright, "Material Characterization of Fused Deposition Modeling (FDM) ABS by Designed Experiments," ed: *Society of Manufacturing Engineers*, 2001.
- [27] L. Novakova-Marcincinova and J. Novak-Marcincin, "Verification of Mechanical Properties of ABS Materials Used in FDM Rapid Prototyping Technology," vol. 8, ed: *Proceedings in Manufacturing Systems*, 2013, pp. 87-92.

- [28] J. F. Rodriguez, J. P. Thomas, and J. E. Renaud, "Mechanical behavior of acrylonitrile butadiene styrene (ABS) fused deposition materials. Experimental investigation," vol. 7, ed: Emerald Insight, 2001.
- [29] Q. Sun, G. M. Rizvi, C. T. Bellehumeur, and P. Gu, "Effect of processing conditions on the bonding quality of FDM polymer filaments," vol. 14, ed. Rapid Prototyping Journal: Emerald Insight, 2008.
- [30] Stratasys. (2016). *3D Printing Solutions | Stratasys*. Available: <http://www.stratasys.com/>
- [31] H. 3D. (2016). *Hyrel 3D*. Available: <http://www.hyrel3d.com/>
- [32] "3d Printing Basics," 2011. [online]. Available: <http://www.3ders.org//3d-printing-basics.html>. Accessed: Jan. 31, 2017.
- [33] Tech-Faq. (2016). *What is Stereolithography?* Available: <http://www.tech-faq.com/stereolithography.html>
- [34] Filabot, "Customer Reviews," 2016. [online]. Available: <https://www.filabot.com/collections/filabot-core/products/filabot-original?variant=570433109>. Accessed: Jan. 31, 2017.
- [35] L. Novakova-Marcincinova and J. Novak-Marcincin, "Verification of Mechanical Properties of ABS Materials Used in FDM Rapid Prototyping Technology," vol. 8, ed: Proceedings in Manufacturing Systems, 2013, pp. 87-92.
- [36] H. K. Garg and R. J. Singh, "Comparison of wear behavior of ABS and Nylon 6—Fe powder composite parts prepared with fused deposition modelling," ed: Central South University Press and Springer-Verlag Berlin Heidelberg 2015, 2015.
- [37] P. J. Nuñez, A. Rivas, E. Garcia-Plaza, E. Beamud, and A. Sanz-Lobera, "Dimensional and Surface Texture Characterization in Fused Deposition Modelling (FDM) with ABS plus," vol. 132, ed. Procedia Engineering: Elsevier, 2015, pp. 856-863.
- [38] M. Dawoud, I. Taha, and S. J. Ebeid, "Mechanical behaviour of ABS: An experimental study using FDM and injection moulding techniques," vol. 21, ed. Journal of Manufacturing Processes: Elsevier and Science Direct, 2016.
- [39] R. Design, and Education for Additive Manufacturing Systems (DREAMS) Laboratory. (2016). *Laser Sintering*. Available: <http://www.me.vt.edu/dreams/laser-sintering/>
- [40] N. S. A. Bakar, M. R. Alkahari, and H. Boejang, "Analysis on fused deposition modelling performance," vol. 11, ed. Journal of Zhejiang University - SCIENCE A: Zhejiang University and Springer-Verlag Berlin Heidelberg 2010, 2010, pp. 972-977.
- [41] D. Espalin, J. A. Ramirez, F. Medina, and R. Wicker, "Multi-material, multi-technology FDM: exploring build process variations," ed. Rapid Prototyping Journal: Emerald Group Publishing Limited, 2013.

Appendices

Appendix A: G-Code for Single-Bar Prints

Slic3r Program

Variations between H and V that are edited after slicing:

- Vertical bars have 68.85% fan. Horizontal bars have 5% fan.
- Vertical bars have a skirt that is as high as the bar, Horizontal bars have a 1 layer skirt.
- Vertical bars have the macro turn all skirt commands above the first layer into a "G0" command, so the print head will move there, but will not extrude any filament.
- Vertical bars have a 150 mm/s skirt travel speed.

```
; avoid_crossing_perimeters = 1
; bed_shape = 0x0,275x0,275x225,0x225
; bed_temperature = 100
; before_layer_gcode = ;announce new layer <[layer_num]>\n;---\nM756 S[layer_height]\nM790
;execute any new layer actions\n;---
; bridge_acceleration = 0
; bridge_fan_speed = 27
; brim_width = 3
; complete_objects = 0
; cooling = 0
; default_acceleration = 0
; disable_fan_first_layers = 1
; duplicate_distance = 6
; end_gcode = M107 T10 ; turn off fans and lasers\nM104 S0 ; turn off temperature\nM140 S0
;turn off the hot bed.\nG91 ;\nG1 Z5.0 ; Drop bed 5mm for extra clearance \nG90
; absolute\nG28 X0 Y0 ; home X axis\nG92 X0 Y0 ; confirm we are at zero\nM84 ;
disable motors\nM30 ; End ofprogram
; extruder_clearance_height = 20
; extruder_clearance_radius = 20
; extruder_offset = 0x0,0x0,0x0,0x0
; extrusion_axis = E
; extrusion_multiplier = 1,1,1
; fan_always_on = 1
; fan_below_layer_time = 60
; filament_colour = #FFFFFF
; filament_diameter = 1.72,1.72,1.72
; first_layer_acceleration = 0
; first_layer_bed_temperature = 100
; first_layer_extrusion_width = 0.4
```

```

; first_layer_speed = 12.5
; first_layer_temperature = 237,237,237
; gcode_arcs = 0
; gcode_comments = 1
; gcode_flavor = reprap
; infill_acceleration = 0
; infill_first = 0
; layer_gcode =
; max_fan_speed = 70
; max_print_speed = 150
; max_volumetric_speed = 0
; min_fan_speed = 27
; min_print_speed = 10
; min_skirt_length = 0
; notes =
; nozzle_diameter = 0.35,0.35,0.35,0.35
; only_retract_when_crossing_perimeters = 1
; ooze_prevention = 0
; output_filename_format = [input_filename_base].gcode
; perimeter_acceleration = 0
; post_process =
; pressure_advance = 0
; resolution = 0
; retract_before_travel = 2,2,2,2
; retract_layer_change = 1,1,1,1
; retract_length = 0,0,0,0
; retract_length_toolchange = 0,0,0,0
; retract_lift = 125,125,125,125
; retract_restart_extra = 0,0,0,0
; retract_restart_extra_toolchange = 0,0,0,0
; retract_speed = 20,20,20,20
; skirt_distance = 10
; skirt_height = 600
; skirts = 1
; slowdown_below_layer_time = 2
; spiral_vase = 0
; standby_temperature_delta = -5
; start_gcode = M104 T10 S[temperature]\nG21 ; use millimeters\nG90 ; absolute
coordinates\nG0 Z5 ; lift head to avoid collisions\nG28 X0 Y0 ; home X and Y\nG92 X0 Y0 ;
reset origin: X and Y\nG0 X0 Y0 ; move to desired origin\nG92 X0 Y0 ; reset origin: X and

```

```
Y\nM83      ; relative extruder coordinates\nM109 S[temperature] ;wait for temperture to  
come up.\nM756 S[first_layer_height] ;set flowfor the first layer please\n\n; temperature = 237,237,237  
; threads = 8  
; toolchange_gcode =  
; travel_speed = 30  
; use_firmware_retraction = 0  
; use_relative_e_distances = 0  
; use_volumetric_e = 0  
; vibration_limit = 0  
; wipe = 0,0,0,0  
; z_offset = 0  
; dont_support_bridges = 0  
; extrusion_width = 0.4  
; first_layer_height = 0.2  
; infill_only_where_needed = 0  
; interface_shells = 0  
; layer_height = 0.2  
; raft_layers = 0  
; seam_position = aligned  
; support_material = 0  
; support_material_angle = 0  
; support_material_contact_distance = 0.2  
; support_material_enforce_layers = 0  
; support_material_extruder = 1  
; support_material_extrusion_width = 0  
; support_material_interface_extruder = 1  
; support_material_interface_layers = 3  
; support_material_interface_spacing = 0  
; support_material_interface_speed = 100%  
; support_material_pattern = pillars  
; support_material_spacing = 2.5  
; support_material_speed = 200  
; support_material_threshold = 0  
; xy_size_compensation = 0  
; bottom_solid_layers = 0  
; bridge_flow_ratio = 1  
; bridge_speed = 12.5  
; external_fill_pattern = rectilinear  
; external_perimeter_extrusion_width = 0.4
```

```
; external_perimeter_speed = 12.5
; external_perimeters_first = 0
; extra_perimeters = 1
; fill_angle = 45
; fill_density = 100%
; fill_pattern = rectilinear
; gap_fill_speed = 12.5
; infill_every_layers = 1
; infill_extruder = 1
; infill_extrusion_width = 0.4
; infill_overlap = 50%
; infill_speed = 12.5
; overhangs = 1
; perimeter_extruder = 1
; perimeter_extrusion_width = 0.4
; perimeter_speed = 12.5
; perimeters = 1
; small_perimeter_speed = 12.5
; solid_infill_below_area = 0
; solid_infill_every_layers = 0
; solid_infill_extruder = 1
; solid_infill_extrusion_width = 0.55
; solid_infill_speed = 15
; thin_walls = 1
; top_infill_extrusion_width = 0.55
; top_solid_infill_speed = 15
; top_solid_layers = 0
```

Macro G-Code Editor Script

```
Sub Skirt_Mover_LM()
'
' Macro1 Macro
'
' Keyboard Shortcut: Ctrl+t
'
'moving skirt 100mm back in the Y direction
'
Dim i As Integer
Dim X As Integer
Dim cellcopy As String
```

```
Dim Xstring As String
Dim XstringInt As Integer
Dim XstringInt2 As Integer
Dim Xstring2 As String
Dim cellcopy2 As String
Dim cellcopy3 As String
```

```
Dim XstringE As String
Dim XstringIntE As Integer
Dim XstringInt2E As Integer
Dim Xstring2E As String
```

```
'fixing extrusion while moving to perimeter point
```

```
'L = 14, M = 14, R=13
'L= 58, M=59, R = 58
```

```
Dim cellcopyB As String
Dim cellcopyC As String
Dim cellcopyD As String
Dim cellcopyE As String
Dim cellcopyF As String
Dim cellcopyG As String
Dim cellcopyH As String
```

```
X = 25000
```

```
For i = 1 To X
```

```
  If InStr(Cells(i, 1), "skirt") Then
    cellcopy = Cells(i, 1)
    Xstring = Mid(cellcopy, 14, 1)
    XstringInt = CInt(Xstring)
    XstringInt2 = XstringInt + 10
    Xstring2 = CStr(XstringInt2)
    cellcopy2 = Replace(cellcopy, Xstring, Xstring2, 14, 1)
```

```
    If XstringInt2 = 0 Then
      cellcopy2 = Replace(cellcopy2, Xstring2, "", 1, 1)
    End If
```

```
    cellcopy3 = Left(cellcopy, 13) & cellcopy2
    Cells(i, 1).Value = cellcopy3
  End If
```

```
,  
,  
,  
,  
  
If InStr(Cells(i, 1), "move to first perimeter point") And InStr(Cells(i + 1, 1), "move to first perimeter  
point") And InStr(Cells(i + 2, 1), "move to first perimeter point") And InStr(Cells(i + 3, 1), "move to first  
perimeter point") Then
```

```
    cellcopyC = Cells(i, 1)  
    cellcopyD = Cells(i + 4, 1)  
    Cells(i, 1).Value = "G0" & Right(cellcopyC, 59)  
    Cells(i + 1, 1).Value = ""  
    Cells(i + 2, 1).Value = ""  
    Cells(i + 3, 1).Value = ""
```

```
    XstringE = Mid(cellcopyD, 14, 2)  
    XstringIntE = CInt(XstringE)  
    XstringInt2E = XstringIntE + 0  
    Xstring2E = CStr(XstringInt2E)  
    cellcopy2E = Replace(cellcopyD, XstringE, Xstring2E, 14, 1)
```

```
    Cells(i + 4, 1).Value = "E0 " & Left(cellcopyD, 13) & cellcopy2E
```

```
    cellcopyG = Cells(i + 4, 1)
```

```
    XstringG = Mid(cellcopyG, 8, 3)  
    XstringIntG = CInt(XstringG)  
    XstringInt2G = XstringIntG + 5  
    Xstring2G = CStr(XstringInt2G)  
    cellcopy2G = Replace(cellcopyG, XstringG, Xstring2G, 8, 1)
```

```
    Cells(i + 4, 1).Value = Left(cellcopyG, 7) & cellcopy2G
```

```
End If
```

```
    If InStr(Cells(i, 1), "move to first perimeter point") And InStr(Cells(i + 1, 1), "move to first perimeter  
point") And InStr(Cells(i + 2, 1), "move to first perimeter point") And InStr(Cells(i + 3, 1), "move to first  
perimeter point") Then
```

```
        End If
```

```
Next i
```

```
End Sub
```

Appendix B: DSC

Thermographs of Functionalized Steel

The two types of functionalized powders that were produced were created in a mixture of water and ethanol (ABS-SS10we) and a mixture of water and hexane (ABS-SS10wh). When the functionalized composites were compared to non-functionalized ABS-SS, functionalized ABS-SS composites showed higher heat capacities and glass transitions at lower temperatures. These results can be seen in the heating and cooling thermographs in Figures C1 and C2. Through functionalized steels, ABS-SS composites may be able to reach a glass transition at lower temperatures while retaining similar thermal and mechanical properties to ABS. This finding shows potential for future research on functionality of polymer-metal composites.

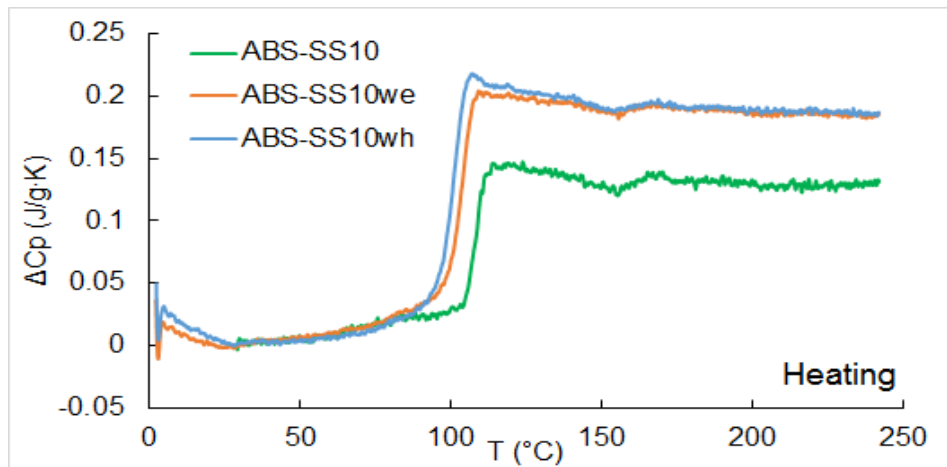


Figure B1: Graph that compares the change in heat capacity of normal ABS-SS10 to ABS-SS10 using functionalized steel during a heating cycle.

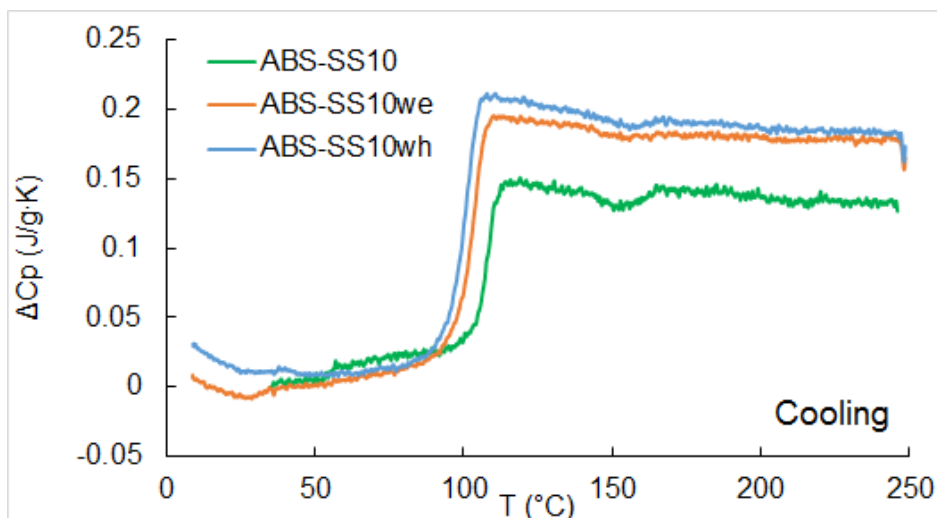


Figure B2: Graph that compares the heat capacity of normal ABS-SS10 to ABS-SS10 using functionalized steel during a cooling cycle.

Heating and Cooling Numerical Data from DSC Tests

The “Scan” column of the following two tables represents which heating or cooling run that the data set is from. “H3” would mean that the data was from the third heating run, while “C2” would mean that the data was from the second cooling run. These runs were providing reproducible data.

Table C1: Heating DSC Data for ABS and PMC Samples.

Sample	Mass [mg] (Mass of ABS) [mg]	Scan	[g/gK]	T _{min} [°C]	T _g [°C]	T _{max} [°C]
Raw ABS	11.00	H2	0.2405	103.72	106.79	109.67
Proc. ABS	11.30	H2	0.1813	106.31	108.42	110.81
Red ABS	11.03	H2	0.3144	97.34	101.65	105.14
SS23	11.00 (8.47)	H3	0.0986	108.68	109.60	112.42
SS15	11.14 (9.47)	H3	0.1912	105.39	109.47	110.92
SS10	11.68 (10.51)	H2	0.1928	106.93	109.24	110.56
SS05	11.00 (10.45)	H3	0.1665	103.63	106.57	110.61

Table B2: Cooling DSC Data for ABS and PMC Samples

Sample	Mass [mg] (Mass of ABS) [mg]	Scan	[g/gK]	T _{min} [°C]	T _g [°C]	T _{max} [°C]
Raw ABS	11.00	C2	0.2469	103.06	107.67	110.18
Proc. ABS	11.30	C2	0.1576	106.13	108.45	110.06
Red ABS	11.03	C2	0.3068	97.12	100.92	105.17
SS23	11.00 (8.47)	C3	0.0780	106.78	108.88	111.31
SS15	11.00 (9.47)	C3	0.1649	105.70	108.09	110.69
SS10	11.68 (10.51)	C2	0.1809	106.42	109.36	110.85
SS05	11.00 (10.45)	C3	0.1800	102.81	106.87	110.28

Nylon-6 Thermograph

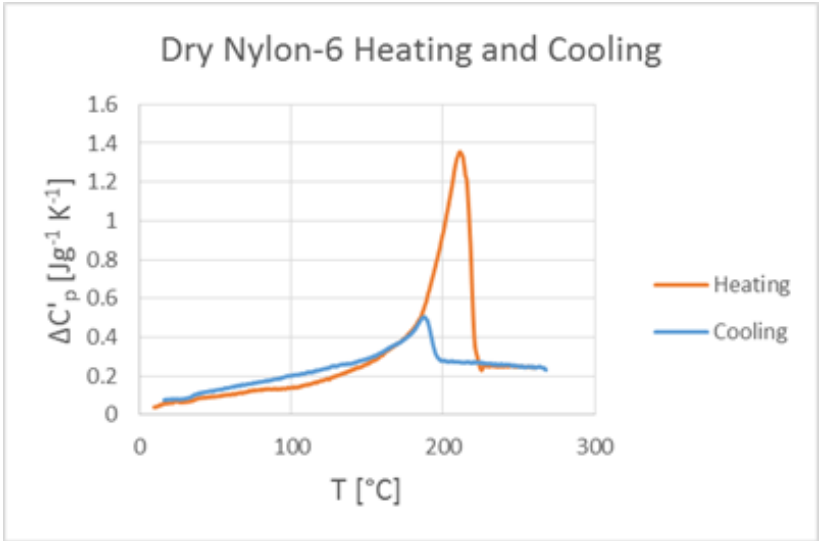


Figure B3: The results of heat capacity during the heating and cooling cycle of dried Nylon-6.

Appendix C: Explorations with Nylon-6

Nylon seems to be only successfully/regularly reinforced with fibrous materials, i.e. Kevlar and or carbon nanotubes. This proves to always be somewhat successful in increasing mechanical properties. Kevlar was added to the printed structure of nylon-6. It was found that the tensile bars with the most Kevlar added had the highest UTS, as seen in Figure A1 [19].

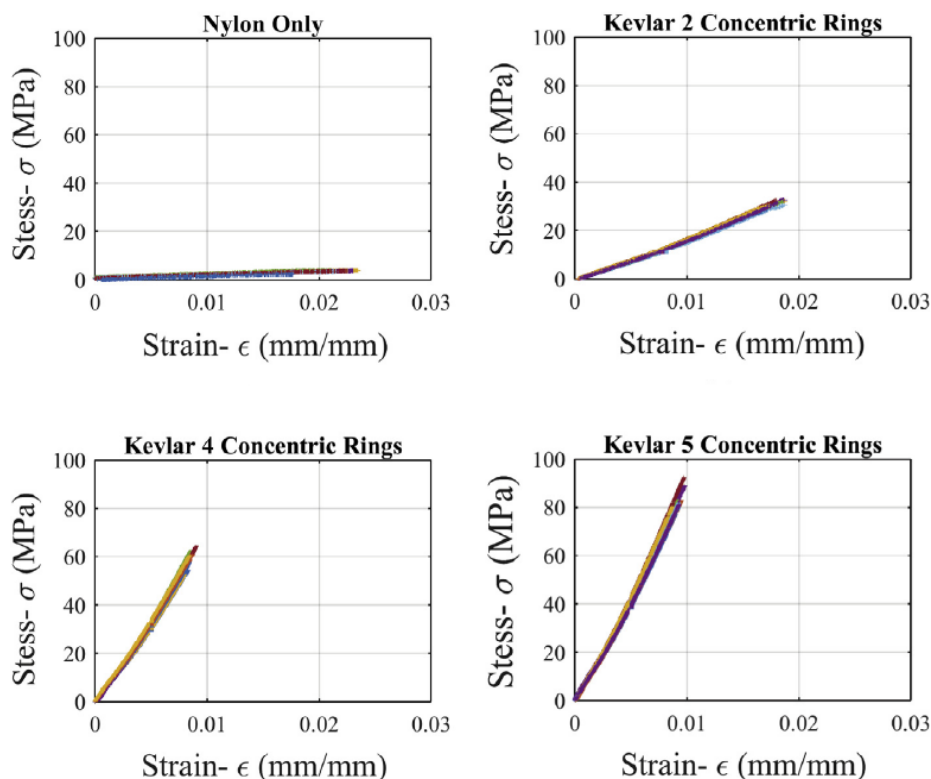


Figure C1: Stress-Strain curves for the four Kevlar fiber reinforcement configurations [19].

Certain concentrations of carbon multi-walled nanotubes (MWNT) were added to the nylon-6 matrix. The composites were tested with differential scanning calorimetry (DSC) to determine the MWNT's effect on the melting behavior of nylon-6. It was determined that the higher amounts of MWNT in the nylon-6 matrix led to heat flow lower than the native material [20].

Nylon has been paired with metals and ceramics like Aluminum and Aluminum oxide. However, it has been shown that these composites fail to better the properties of plain nylon. The common issue in adding metals or ceramics to the nylon matrix is that the added filler does not completely wet in the matrix. Nylon-6 (E-35 grade) was selected as the binding material for the composites created in this experiment. Aluminum and aluminum oxide were used as fillers in the nylon-6 matrix to test for their effect on the native material's tensile properties. Aluminum's self-lubricating properties proved it to have good binding properties with nylon-6; not surfactants or plasticizers were needed. A single-screw extruder was selected for the creation of the composite filaments. The filaments were then tensile tested to ASTM-638 standard. It was found that the

tensile strength of the binder material decreases with addition of filler to its matrix [21]. Increasing the amount of wetting between the base polymer matrix and filler material could lead to an increase in the composite mechanical properties. To create better wetting between the materials in question, the use of surface modifying agents is vital. Noting that aluminum mixes well with nylon-6, we can focus on different attributes in the processing of the polymer-metal composite such that the product will have increased mechanical properties. Certain concentrations of carbon multi-walled nanotubes (MWNT) were added to the nylon-6 matrix. The composites were tested with differential scanning calorimetry (DSC) to determine the MWNT's effect on the melting behavior of nylon-6. It was determined that the higher amounts of MWNT in the nylon-6 matrix led to heat flow lower than the native material [19].

Appendix D: Average Tensile Data Tables

Table D1: Comparing averages from tensile tests of the 0/90 H prints of each material

0/90 H						Units
Set of Bars	Factory ABS	Raw ABS	ABS-SS10	ABS-SS15	ABS-SS23	
Max Load	395.577	394.327	387.576	346.603	271.501	N
UTS	37.858	40.419	36.733	33.268	26.514	MPa
YS	33.460	30.740	31.170	27.024	21.214	MPa
E	0.749	0.666	0.709	0.684	0.640	GPa
Ductility	29.693	28.415	27.501	20.818	22.266	%
Extension	0.297	0.284	0.275	0.208	0.223	m

Table D2: Comparing averages from tensile tests of the -45/45 H prints of each material

-45/45 H						Units
Set of Bars	Factory ABS	Raw ABS	ABS-SS10	ABS-SS15	ABS-SS23	
Max Load	385.078	394.362	379.720	372.936	250.782	N
UTS	38.313	40.054	33.914	37.118	24.490	MPa
YS	29.425	28.960	28.131	31.031	20.287	MPa
E	0.743	0.667	0.656	0.720	0.568	GPa
Ductility	30.821	26.982	22.417	12.258	29.000	%
Extension	0.308	0.270	0.224	0.123	0.290	m

Table D3: Comparing averages from tensile tests of the 0/90 V prints of each material

0/90 V						Units
Set of Bars	Factory ABS	Raw ABS	ABS-SS10	ABS-SS15	ABS-SS23	
Max Load	382.017	365.180	354.510	317.676	198.039	N
UTS	31.342	30.426	29.078	29.090	18.347	MPa
YS	23.613	22.224	19.774	24.857	15.094	MPa
E	0.672	0.575	0.613	0.605	0.539	GPa
Ductility	7.750	7.740	8.691	6.659	7.889	%
Extension	0.078	0.077	0.087	0.067	0.079	m

Table D4: Comparing averages from tensile tests of the -45/45 V prints of each material

Comparing Averages: -45/45 V						Units
Set of Bars	Factory ABS	Raw ABS	ABS-SS10	ABS-SS15	ABS-SS23	
Max Load	391.377	382.490	311.338	317.033	184.822	N
UTS	31.478	30.989	25.773	26.257	14.762	MPa
YS	24.248	21.740	20.287	21.114	11.603	MPa
E	0.678	0.573	0.626	0.622	0.448	GPa
Ductility	8.819	5.542	6.968	6.285	8.064	%
Extension	0.088	0.092	0.070	0.063	0.081	m

